공학석사 학위논문

Virtual RTM Manufacturing Simulation of Carbon-Fiber Reinforced Laminate Composites Using a Probabilistic Thermochemical Viscoelastic Model

확률적 열화학 점탄성 모델을 적용한 탄소섬유 강화 적층 복합재료의 가상 RTM 제조 시뮬레이션

2020 년 8 월

서울대학교 대학원

항공우주공학과 항공우주공학전공

블랑코 로자스

Virtual RTM Manufacturing Simulation of Carbon-Fiber Reinforced Laminate Composites Using a Probabilistic Thermochemical Viscoelastic Model

확률적 열화학 점탄성 모델을 적용한 탄소섬유 강화 적층 복합재료의 가상 RTM 제조 시뮬레이션

지도 교수 윤 군 진

이 논문을 공학석사 학위논문으로 제출함
2020 년 8 월

서울대학교 대학원
항공우주공학과 항공우주공학전공
블랑코 로자스

블랑코 로자스의 공학석사 학위논문을 인준함
2020 년 8 월

위 원 장 신 상 준 (인)

부위원장 윤 군 진 (인)

위 원 김 용 협 (인)

본 논문작성자는 한국정부초청장학금 **(Global Korea Scholarship)**을 지원받은 장학생임

Abstract

Virtual RTM Manufacturing Simulation of Carbon-Fiber Reinforced Laminate Composites Using a Probabilistic Thermochemical Viscoelastic Model

Sebastian Leonardo Blanco Rojas
Department of Aerospace Engineering
Aerospace Engineering Major
The Graduate School
Seoul National University

Composite materials undergo a shrinkage process related to the curing kinetics of the matrix. This shrinkage effect, added to the material thermal expansion, results in geometric distortions and residual interlaminar stresses that affect negatively the mechanical response of the materials.

This work addresses the effects of the manufacturing process on carbon fiber reinforced composite laminates used in aerospace structures. Here,

computational tools are implemented to model a viscoelastic material with degree of cure and time-dependent properties. Additionally, probabilistic modeling tools are implemented in the interest of increasing the reliability of the results by considering the random nature of curing kinetics parameters.

The model consists of a multiphysics system that couples the thermochemical and mechanical processes. First, the heat transfer analysis is performed by relating Fourier's heat conduction governing equations with Kamal's model of curing kinetics. Then, for the mechanical analysis, a 9-element Generalized Maxwell Model is implemented to compute the viscoelastic behavior. The representation of a cure and time-dependent viscoelastic model is possible due to the thermorheologically simple nature of the thermosetting resins. Here, a shift factor is applied to obtain stress relaxation times that change with the temperature and the degree of cure of the material. To produce the stochastic behavior of the materials, random fields were created by implementing the Karhunen-Loève Expansion method with a Monte Carlo simulation.

The manufacturing method consisted of a vacuum-assisted transfer molding (VARTM) with a post-curing treatment. To emulate this

process, the mechanical and thermal boundary conditions are divided into four stages. The first one refers to the curing stage. Here, the plate is constrained in the mold and subjected to thermal conduction in the surfaces. The second stage is when the plate is released from the mold and left to cool down to room temperature by natural convection. The third stage consists of placing the cooled plate into an oven (forced thermal convection). Finally, the plate is left to cool down as in the second stage. The stress and distortions that result from this manufacturing process were analyzed in six plates with different ply configurations.

The results showed that the quasi-isotropic laminate $[-60/-30/0/30/60/90]$ undergoes the highest interlaminar stresses and distortions, followed by the asymmetric cross-ply laminate $[90_3/0_3]$. It also revealed that the post-curing process increases the interlaminar residual stresses in most of the laminates, especially in the case of the antisymmetric angle ply laminate.

The effect of the cure dependent viscoelastic model is then compared to a basic linear elastic material response. Revealing that a viscoelastic model predicts higher stresses during the curing stage (in-mold plates) but lower stresses once the plates are released from the molds. Finally,

the effects of taking into account the random nature of the curing kinetics parameters were observed in the curing stage of a cross-ply laminate. This analysis revealed that the stresses can be 23.86% higher than the values predicted from a viscoelastic model that ignores this effect. Demonstrating the importance of considering the random nature of the properties involved in the curing process.

Keywords: Viscoelasticity, curing kinetics, composite laminates, residual stress, laminate distortions, finite element analysis, stochastic behavior, random field.

Student Number: 2018-27407

Contents

List of Tables

List of Figures

Chapter 1. Introduction

During the last decades the aerospace industry has been experiencing a constant shift from the use of traditional materials to more advanced composites. The improvement of manufacturing strategies is one of the most important reasons for this change. During the manufacturing process, the properties mismatch of composite materials results in residual stresses buildup and geometrical variations of the final structures, especially because of the chemical shrinkage and thermal expansion of the thermoset epoxies that conform the matrix. The magnitude of the stresses and deformations depends on the laminate configuration and the process itself. High residual stresses lead to a decay in the structure performance and large deformations result in manufacturers overwork, increasing the production cost. This is why predicting the behavior of a composite structure during the manufacture is crucial. However, it is complicated, and in some cases, the experimental approach is not a viable option. Consequently, computational tools have become a paramount need in this area. A reliable computational model must take into account the mechanics of the materials and the thermodynamics in each manufacturing stage.

1.1 Aerospace Industry Materials

One of the most important criteria to be considered in engineering design is the material selection. The value of the materials used in an aerospace structures depends on the performance, production cost, lifecycle management and environmental impact [1]. The materials commonly used today can be divided into four basic categories: metals, polymers, ceramics and composites[2]. Light metals like aluminum or titanium are popular among the designers due to its capacity to reduce the weight of the aerostructures. The use of metallic components can be traced back to the aluminum body of the Zeppelin in the early years of the aerospace industry [3]. The development of new metallic alloys expanded the application of these materials. A good example is the titanium nitride (TiN), a wear-resistant coating material used in the Cassini Langmuir probe [4]. The addition of aluminum to this alloy can improve the mechanical properties for satellites near the atmosphere of the Earth [5]. Likewise, some satellite cooling systems implement titanium alloys joined to stainless steel [6]. In the case of the composite materials, the first industrial composites used in aircrafts were the glass-fiber reinforced polymer laminates. Initially, these composites were limited to

few components because of the poor mechanical properties of the fibers. However, the development of better resins and fibers resulted in a greater variety of applications in the new generation aero-vehicles [7]. Combat aircrafts like the Lockheed Martin F-35 Lightning II or the Unmanned Combat Air Vehicles (UCAV) and civil airplanes like the Boeing 787 Dreamliner or the Airbus A350 are excellent examples of how the composite materials usage in the aerostructures has escalated dramatically during the last decades [8]. Several components of the iconic Airbus A380, including the outer flaps, spoilers and ailerons, the engine cowlings and the upper deck floor beams are made of a particular composite material: Carbon Fiber Reinforced Polymers (CFRP) [7]. CFRP components can be found in different structural configurations. Cutting-edge examples are the stiffened panels used in the fuselage of the 787 Dreamliner and the deployable payload fairings of launch vehicles [9]. The design of modern aerostructures comprise the development of biomimetics as a way to create new technologies based on the understanding of biological principles. Likewise, the novel manufacture techniques apply Artificial Intelligence (AI) to their processes [10].

1.2 Composite Materials

Composites consist of a combination of two materials with different mechanical properties. This combination gives the designers the opportunity to obtain materials with properties that cannot be found in any other of the constituent materials acting alone [2]. Composites offer a superior strength to weight ratio. This reduces the weight of the structures while enhancing the performance of the aero-vehicles [10].

Examples of man-made composite structures can be listed from ancient straw-reinforced clay bricks to modern composites such as the CFRP. The CFRP consist of reinforcement materials (strong carbon fibers) set in a matrix of filler materials (plastics or epoxies) that work as lightweight energy-absorbing protective shields [11]. The reinforcement materials in general composites are high modulus fibers, such as boron, silicon carbide, graphite, Kevlar® aramid or carbon fibers. Carbon fibers are made of high strength hexagonal layers of graphite crystallites and are commonly 6 μm in diameter [12]. Some examples of aerospace grade specification fibers include polyacrylonitrile (PAN) based carbon fibers that can reach tensile modulus over 140 GPa such as HexTow® AS7, HexTow® AS4C or HexTow® IM7 [13]. The filler materials, on the

other side, consist mostly of lightweight polymers that give structural unit, protection and distribute applied loads to the fibers [2]. Polymers are divided in two main groups: thermosetting and thermoplastics. Thermosetting materials such as epoxy or polyimide resins undergo an irreversible cross-linking process during the curing stage. Thermoplastic materials such as polymethyl methacrylate (PMMA) or polyether ether ketone (PEEK) have no chemical bonding. Therefore, the curing process is reversible.

Composite materials have been part of the aerostructures since the very beginning. Natural composites like woods or fabrics have been used in some airplanes, good examples are the Wright Brother's Flyer 1 [12] and the "Spruce Goose", the largest wooden airplane ever constructed, made almost entirely of birch despite its name [14]. However, lightweight metallic alloys became the predominant structural materials for several years. The thermoset polymers were introduced in the aerospace industry as adhesives that bonded the wooden frames of the early aircrafts. The first time that thermoset materials were used with structural purposes was in the production of the Supermarine Spitfire [8]. During the past years, the cost reduction in the production of composites and the new

manufacturing technologies resulted in a rapid increase of the popularity of the composite materials over the conventional counterparts.

1.3 Manufacture of Composite Materials

The main purpose of the manufacture of composite materials is to give an appropriate orientation to the fibers in the matrix while maintaining adequate proportions to obtain a product with optimum mechanical properties [7]. Here, the manufacturing process will be divided into three main groups: open molding, closed molding and continuous process.

Open mold manufacturing techniques are simple and inexpensive processes. Here, resins are exposed to room conditions while cured, these techniques are ideal to create prototypes [15]. A good example of an open mold process is the wet hand lay-up (HL). This is a low tool-cost process [16] in which the fibers are placed by hand and the resin is impregnated with a roller or a brush. Important setbacks to this method are related to the raise of occupational health and safety concerns when handling wet resins and the process lack of repeatability [7].

In the closed mold manufacturing process, the fibers and the resin are fully constrained and can be subjected to different pressure and temperature conditions. The most basic example of a closed mold

process is the vacuum bag molding. Here, the resin and fibers are placed into a flexible plastic membrane that generates vacuum. The atmospheric pressure helps to remove the air and volatile materials; it also enhances the mechanical properties of the laminate by compacting the resin and fibers. A variation of this process is the vacuum infusion (VI) method. In this case, the laminates without the resin are placed inside the mold and subjected to vacuum. After this, the resin is injected and uniformly distributed. The main issue of this process is that it can provide limited consolidation pressure [7]. To overcome this obstacle, some processes replace the use of plastic membranes with clamped solid molds. Resin transfer molding (RTM) is a popular closed mold manufacturing process. Here, woven fiber plies are used to achieve better structural performance. In order to fill the empty spaces of the woven plies, high pressure and low-density resins that could be injected between the fibers are required. Because of this, thermosetting epoxies are commonly used in this process. The resin transfer can also be assisted by applying vacuum to the exhaust. This variation is known as the vacuum assisted resin transfer molding (VARTM). This process has the advantages of flexibility and scalability of the HL processes with the benefits of the quality and repeatability od the RTM [17]. RTM processes are limited to simple

geometry parts. If the shape of the product includes complex features, compress molding is a more suitable method.

The continuous manufacturing processes consist on system where the fibers and resins are fed constantly. A conventional technique is the filament winding. Here, a continuous fiber strand is fed to a resin container where the fibers are impregnated with resin while a rotating mandrel forms the inner surface of the part. In the early years, rocket components and other axially symmetrical parts were manufactured by using this technique [17]. Another cost-effective continuous process is the pultrusion. This technique is similar to the metallic extrusion used in the manufacturing of aircraft stringers [12]. Here, a strand of fiber is constantly pulled through a steel die that shapes the product.

Reducing energy consumption and increasing the product output are paramount needs in the composite manufacturing industry. As a consequence, different variations of the traditional processes are constantly being tested. This includes reinforced reaction injection molding (RRIM) coupled with pultrusion, high-speed RTM and instantaneous induction heating of the mold surface [8]. The composite manufacturing industry faces the process-related distortions and residual stresses inherent to the dynamic of the fibers and epoxies, especially

during the curing and cooldown stages. Experimental testing tends to be expensive and the results are not reliable in many cases. Because of this, virtual modeling is gaining popularity as an ally in the understanding and improvement of the composite manufacturing process.

1.4 Previous Research

Several authors have studied the process-induced distortions and residual stress in antisymmetric layup configuration laminates [18-20]. Other studies relate the laminate warpage and the "spring in" effect of curved "L" or "C" parts to the thermal deformations that rise during the curing process [21]. Among the experimental methods to be accounted for, some studies have included fiber optic sensors[22] and interrupted warpage tests [23] during the curing process. Others have used destructive methods after the curing, such as the hole drilling method [24]. Tool-part interaction has been widely studied [25]. Multiscale models have been proposed to observe the effect of different boundary conditions over the residual stresses [26]. Chen et al. proposed an Extended Concentric Cylinder Assemblage (ECCA) model to compute the effective lamina responses [27]. Degree of cure and temperature-dependent viscoelastic models are used to produce the material stress

relaxation during the cure [28]. While some authors have incorporated a light scattering method to obtain cure-dependent properties for the curing matrix [29]. The classical lamination theory (CLT) has been used for the calculation of residual stress in each layer of laminated composites [24]. Studies on the effects of the interaction between different laminate configurations and aluminum plates have been used to improve the prediction of residual stresses [30]. Besides, the rise of distortions of a fully cured laminate subjected to a post-curing process has been investigated by several authors [31-33].

1.5 Thesis Structure

This work is divided into six sections. Following the introduction in Chapter 1, important background information related to the model used is given in Chapter 2. This section covers the thermochemical and viscoelastic models coupled in the analysis. It also includes the literature review on the cure dependency of some properties, the random field generation of stochastic parameters and the Classical Lamination Theory. In Chapter 3, the details of the methodology and the material properties are given. Chapter 4 consists on the experimental validation of the proposed model. Chapter 5 refers to the analysis of results. Chapter 6

presents the conclusions and final discussion. The information given in the appendix is related to the classical lamination theory and the computational codes used in this work.

Chapter 2. Literature Review

2.1 Thermochemical Model

The thermochemical behavior of a thermoset polymer can be modeled by coupling the degree of cure kinetics with the material heat conductivity formulation [34]. The parameters that define the degree of cure (α) are commonly obtained from Differential Scanning Calorimetry (DSC). This analytical approach defines α as the ratio of the energy released at a time t to the total heat of reaction.

$$\alpha(t) = \frac{H_t}{H_m} \tag{2.1}$$

Where, H_t and H_m are the heat release at a time t and the total heat of reaction respectively.

In 1974, Musa R. Kamal [35] presented a semi-empirical model that describes the degree of cure rate $(\frac{\partial \alpha}{\partial t})$ appropriately

$$\frac{\partial \alpha}{\partial t} = (K_1 + K_2 \alpha^m)(1 - \alpha)^n \tag{2.2}$$

In this equation, superscripts m and n refer to temperature independent reaction orders and K_i are temperature-dependent reaction rates that commonly take the form of Arrhenius equation as [36]

$$K_i = A_i \exp\left(\frac{-E_i}{RT}\right), \qquad \mathrm{i} = 1,2,3 \tag{2.3}$$

The Arrhenius parameters A_i and ΔE_i indicate the frequency factor and the activation energy; R is the universal gas constant. Sensitive tests have revealed that the Arrhenius coefficients cannot be estimated independently when using data from dynamic experiments [37]. The model that best describes the exothermic cure reaction in the Hercules 3501-6 resin is expressed as [38, 39]

$$\frac{\partial \alpha}{\partial t} = \begin{cases} (K_1 + K_2\alpha)(1-\alpha)(0.47-\alpha) & (\alpha \le 0.3) \\ K_3(1-\alpha) & (\alpha > 0.3) \end{cases} \tag{2.4}$$

A governing equation based on Fourier's analytic heat formunation denotes the transient heat conduction of the curing composite as shown [40]

$$\lambda_{\mathrm{x}} \frac{\partial^2 T}{\partial x^2} + \lambda_{\mathrm{y}} \frac{\partial^2 T}{\partial y^2} + \lambda_{\mathrm{z}} \frac{\partial^2 T}{\partial z^2} + Q = \rho_{\mathrm{c}} C_c \frac{\partial T}{\partial t} \tag{2.5}$$

Here, λ_i, $i = x, y, z$ refers the anisotropic heat conductivities in x, y, and z-direction; T is the transient temperature field at time t; ρ_c is the composite density and C_c is the specific heat capacity. The internal heat

generation of the composite Q, related to the resin polymerization α is given by

$$Q = \rho_m(1 - V_f)H_m \frac{\partial \alpha}{\partial t} \tag{2.6}$$

Where H_m is the total energy of reaction of the thermosetting polymer introduced in (2.1); ρ_m is the density of the resin matrix and V_f refers to the volume fraction of the fiber. The composite conductivity parameters are obtained from the rule of mixture given in [26]. In this work, isotropic conductivity of the resin and transversely isotropic conductivity of the fiber is assumed [41].

$$\lambda_1 = V_f \lambda_f^L + (1 - V_f)\lambda_m \tag{2.7}$$

$$\frac{\lambda_2}{\lambda_m} = \left(1 - 2\sqrt{V_f/\pi}\right) + \frac{1}{X}\left[\pi - \frac{4}{\sqrt{1 - X^2 V_f/\pi}} \tan^{-1} \frac{\sqrt{1 - X^2 V_f/\pi}}{1 + X\sqrt{V_f/\pi}}\right] \tag{2.8}$$

Where X is obtained from

$$X = 2\left(\frac{\lambda_m}{\lambda_f^T - 1}\right) \tag{2.9}$$

In this equation λ_m indicates the thermal conductivity of the polymer matrix; λ_f^T and λ_f^L are the transverse and longitudinal thermal conductivites of the fiber respectively. The same way, density and specific heat capacity for the composite are given by

$$\rho_c = V_f \rho_f + \left(1 - V_f\right)\rho_m \tag{2.10}$$

$$\mathrm{C_c} = \frac{V_f \rho_f C_f + \left(1 - V_f\right)\rho_m C_m}{\rho_c} \tag{2.11}$$

Where ρ_f is the fiber density; and C_m and C_f are the specific heat capacities of the resin and fiber, respectively.

2.2 Viscoelastic Model

As mentioned in earlier chapters, the filler materials of the composites consist of polymers that give structural unit and protection to the fibers. Polymers are used not only for their lightweight, but because of their characteristic response to external loads. Depending on the circumstances, polymers can be treated as an elastic solid or as a viscous liquid [42]. This unique behavior is known as viscoelasticity.

Viscoelastic materials have been studied for decades, leading to a formulation of different models that can be divided into two main groups: "mechanical analogs" and molecular theories [43]. Mechanical analog models are used to understand the deformation mechanisms of a viscoelastic material subjected to long term loads. These models can represent two important characteristic behaviors of the polymeric materials: the material stress relaxation and the creep compliance [44].

Stress relaxation is a time-dependent decrease in stress under a constant strain. Creep, on the other hand, is the time-dependent increase in strain under a constant stress[45]. The mechanical analog models are presented in the following chapters.

2.2.1 Analog Mechanical Models

The most basic mechanical models consist of simple arrangements of a spring and a dashpot. The spring represents Hooke's relation between load and displacement. In this work, this relation will be labeled with the letter Q. This proportionality constant can be analogous to the Young's Modulus or the Shear Modulus of an elastic solid. The dashpot, on the other hand, represents the shear viscosity relation (η) between load and rate of deformation of a viscous element, used to model a Newtonian fluid[46]. The two basic elements are shown in Figure 2.1.

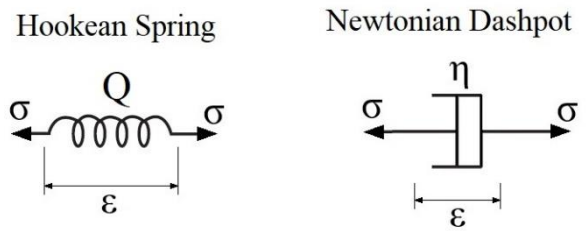

Figure 2.1. Basic Elements

The relaxation functions for the Hookean Spring and the Newtonian Dashpot are defined respectively as:

$$G_s(t) = Q \tag{2.12}$$

$$G_d(t) = \eta\delta(t) \tag{2.13}$$

Where $\delta(t)$ is the Dirac delta function[47].

$$\delta(t) = \frac{dH(t)}{dt} \tag{2.14}$$

Here, $H(t)$ is the Heavyside function and is defined as[42]:

$$H(t) = \begin{cases} 0 & t < 0 \\ 1 & t > 0 \end{cases} \tag{2.15}$$

And the creep compliance functions for both elements are given by:

$$J_s(t) = \frac{1}{Q} \tag{2.16}$$

$$J_d(t) = \frac{1}{\eta}t \tag{2.17}$$

By using these concepts, simple models are built in order to produce the viscoelastic behavior. The two basic arrangements are shown in Figure 2.2.

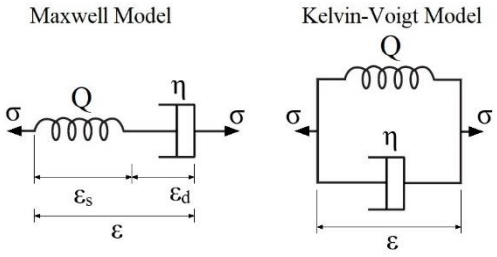

Figure 2.2. Basic Models

The first model is a simple arrangement of a Hookean spring and a Newtonian dashpot in series, known as the Maxwell Model. This configuration has the characteristics of a fluid material; because of this, it is also known as the Maxwell Fluid Model. Note that the stress in both elements has the same value while the total strain is the sum of each component. (i.e.)

$$\sigma = \sigma_s = \sigma_d \tag{2.18}$$

$$\varepsilon = \varepsilon_s + \varepsilon_d \tag{2.19}$$

These equations give the following constitutive law[47]:

$$\dot{\sigma} + \frac{Q}{\eta}\sigma = Q\dot{\varepsilon} \tag{2.20}$$

Where the upper dot (·) refers to the time derivative. It is important to introduce here a widely used parameter known as the relaxation time:

$$\tau = \frac{\eta}{Q} \tag{2.21}$$

By substituting the relaxation time constant, equation (2.20*)* becomes:

$$\dot{\sigma} + \frac{1}{\tau}\sigma = Q\dot{\varepsilon} \tag{2.22}$$

The solution for the differential equation is given by[47]:

$$\sigma = Qe^{\left(\frac{-t}{\tau}\right)}\varepsilon_0 \tag{2.23}$$

Where,

$$\sigma = G(t)\varepsilon_0 \tag{2.24}$$

Hence, the stress relaxation function is:

$$G(t) = Qe^{\left(\frac{-t}{\tau}\right)} \tag{2.25}$$

Maxwell Fluid Model shows an instant elastic deformation, then the strain increases linearly with time under an applied constant stress. The strain is represented by the following equation[42]:

$$\varepsilon(t) = \left(\frac{1}{Q} + \frac{t}{\eta}\right)\sigma_0 \tag{2.26}$$

Where,

$$\varepsilon(t) = J(t)\,\sigma_0 \tag{2.27}$$

Hence, the creep compliance function is:

$$J(t) = \frac{1}{Q} + \frac{t}{\eta} \tag{2.28}$$

Maxwell Fluid Model can characterize the stress relaxation properly but it cannot produce the creep of a viscoelastic material[48].

The second model, known as Kelvin-Voigt Model, is an arrangement of a Hookean spring and a Newtonian dashpot in parallel. This configuration is known as the Kelvin-Voigt Solid Model because it describes the behavior of a solid-like material. In this case, the total stress equals to the summation of each component while the strain in both elements gets the value of the total strain.

$$\sigma = \sigma_s + \sigma_d \tag{2.29}$$

$$\varepsilon = \varepsilon_s = \varepsilon_d \tag{2.30}$$

The constitutive law for this model is:

$$\sigma = Q\varepsilon + \eta\dot{\varepsilon} \tag{2.31}$$

The solution for the differential equation is given by:

$$\varepsilon(t) = \frac{1}{Q}\left[1 - e^{\left(\frac{-t}{\tau}\right)}\right] \sigma_0 \tag{2.32}$$

Here, the creep compliance function is:

$$J(t) = \frac{1}{Q}\left[1 - e^{\left(\frac{-t}{\tau}\right)}\right] \tag{2.33}$$

This model presents a lineal increase of strain with time under an applied constant stress. Kelvin-Voight Solid Model describes the creep and the recovery conditions [48]. However, the dashpot prevents the model to

produce the instant elastic deformation. Therefore, stress relaxation test is not possible under this configuration.

Both of the mentioned models can adequately predict creep and stress relaxation individually. However, they cannot be considered as valid viscoelastic models because of their limitations to produce both behaviors at the same time.

2.2.2 Multiple Element Models

In order to improve analog mechanical modeling, more complex models consisting of arrangements of three or four elements are made as shown in Figure 2.3. The first model is the Maxwell four parameter fluid in which the creep increases without limit over time, under a constant stress applied. Then, in stress relaxation, the value of stress decays to zero. The second model is the Kelvin three parameter solid, where the solid creep has a limit strain and the stress decrement is also limited in stress relaxation[42].

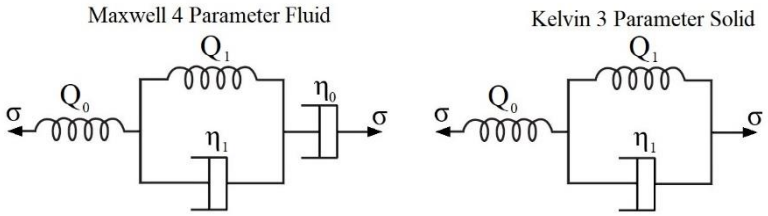

Figure 2.3. Multiple Element Models

2.2.3 Generalized Kelvin Model

The Generalized Kelvin-Voigt Model (GKM) consists on a free spring in series with an arbitrary number of basic Kelvin Elements as shown in Figure 2.4.[49, 50]

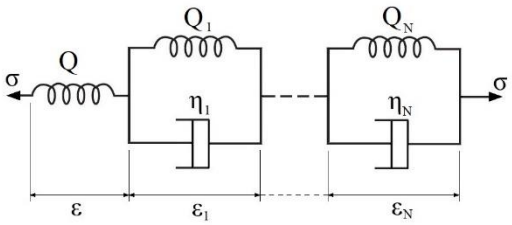

Figure 2.4. Generalized Kelvin-Voigt Model

For this configuration the stress magnitude has the same value at each increment and equals to the stress at the free spring.

$$\sigma = Q\varepsilon = \sigma_i = Q_i\varepsilon_i + \eta_i\dot{\varepsilon}_i \qquad (2.34)$$

Where $\dot{\varepsilon}$ represents the time derivative of strain and $i = 1,2,\ldots,N$. Kelvin elements in series are used for creep determination. The addition of the free spring gives the possibility of obtaining the instantaneous elastic response. Hence, the creep compliance function is

$$J(t) = \frac{1}{Q_0} + \sum_{i=1}^{N} \frac{1}{Q_i}\left[1 - e^{\left(\frac{-t}{\tau_i}\right)}\right] + \frac{t}{\eta_0} \qquad (2.35)$$

2.2.4 Generalized Maxwell Model

The Generalized Maxwell Model, also known as the Wiechert Model consists on a free spring in parallel with an arbitrary number of Maxwell Elements as shown in Figure 5.

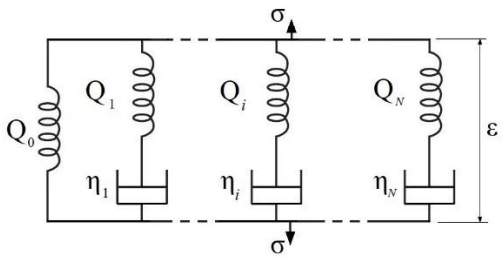

Figure 2.5. Generalized Maxwell Model

For this configuration, the value of the strain is equal in each parallel element and the overall stress is the sum of each individual stress.

$$\varepsilon(t) = \varepsilon_i(t) \qquad (2.36)$$

$$\sigma(t) = \sigma_0(t) + \sum_{i=1}^{N} \sigma_i(t) \qquad (2.37)$$

Where $\sigma_0(t)$ indicates the stress at the free spring and $\sigma_i(t)$ refers to the internal stress at each Maxwell Element. In this model, the order of the differential equation changes with the number of elements used. Several Maxwell elements are needed to produce the stress relaxation of a polymer, leading to high order differential equations. Each one of the differential equations has the following form:

$$\sigma_i(t) + \tau_i \dot{\sigma}_i(t) = \eta_i \dot{\varepsilon}_i(t) \qquad (2.38)$$

Where $\dot{\varepsilon}$ is the time derivative of strain, $\dot{\sigma}$ is the time derivative of stress and $i = 1,2, \dots, N$. The solution of each differential equation gives the relaxation modulus for the Generalized Maxwell Model[42]

$$G(t) = Q_0 + \sum_{i=1}^{N} Q_i e^{\left(\frac{-t}{\tau_i}\right)} \qquad (2.39)$$

For a material incremental strain $\Delta\varepsilon_i$ the relaxation can be expressed as

$$G(t-s) = Q_0 + \sum_{i=1}^{N} Q_i e^{\left(\frac{s-t}{\tau_i}\right)} \qquad (2.40)$$

Where s refers to the initial response time[46]. Then, the Cauchy Stress becomes

$$\sigma(t) = \int_0^t G(t-s)\frac{\partial \varepsilon}{\partial s} ds \qquad (2.41)$$

This equation can be rewritten as

$$\sigma(t) = Q_0\varepsilon(t) + \int_0^t \sum_{i=1}^{N} Q_i e^{\left(\frac{s-t}{\tau_i}\right)} \frac{\partial \varepsilon(s)}{\partial s} ds \qquad (2.42)$$

Then, the stress at the free spring $\sigma_0(t)$ and the internal stresses of each Maxwell Element $\sigma_i(t)$ can be obtained from equation (2.37*)* and equation (2.42*)* as follows

$$\sigma_0(t) = Q_0\varepsilon(t) \qquad (2.43)$$

$$\sigma_i(t) = \int_0^t Q_i e^{\left(\frac{s-t}{\tau_i}\right)} \frac{\partial \varepsilon(s)}{\partial s} ds \qquad (2.44)$$

2.3 Cure and temperature dependence

Thermosetting polymers are considered thermorheologically simple materials. This means that their mechanical responses show a dependency on temperature that is amenable to analytical descriptions [51]. This section examines the modifications needed in the stress-strain relation presented in *(2.42)* to produce a temperature dependent viscoelastic effect considering continuous shifts of temperature.

In a thermorheologically simple material, the material behavior at any temperature *T* can be easily determined if the response is known at a

reference temperature T_0 by simply changing their stress relaxation times (τ) [52]. This is known as the Time Temperature Superposition Principle (TTSP) and is expressed as follows

$$G(t;T) = G(\xi^t - \xi';T_0) \tag{2.45}$$

Where ξ^t and ξ' are the current and past reduced time respectively. These variables are given by

$$\xi^t = \int_0^t \frac{1}{\theta_T(\alpha,T)}\,dt \tag{2.46}$$

$$\xi' = \int_0^s \frac{1}{\theta_T(\alpha,T)}\,ds \tag{2.47}$$

Here, $\theta_T(\alpha,T)$ is a cure and temperature dependent shift function. Studies on aerospace-grade resins have been conducted to obtain the parameters that define this particular function for different epoxies [53-55]. This work focuses on Hercules 3501-6 resin. The parameters and formulation used here are obtained from the works of Lee, W.I. [54] and Kim, Y.K.[56]. The shift function is defined as

$$\theta_T(\alpha,T) = 10^{\left[-a_1 \exp\left(\frac{1}{\alpha-1}\right)-a_2\right][T-T_c]} \tag{2.48}$$

Where a_1 and a_2 are curve fitting parameters with magnitudes of 1.4 and 0.012, respectively and the reference temperature T_c is set to 303 K.

Additionally, a cure dependent stress relaxation is set for this material as follows

$$\tau(\alpha) = 10^{[\log\left(\tau_i(\alpha^0)\right)+(\psi(\alpha)-(\alpha-\alpha^0)\log\,(\lambda_i))]} \tag{2.49}$$

Where $\tau_i(\alpha^0)$ is the peak relaxation time of the i-th Maxwell element at a reference degree of cure where the stress relaxation behavior is known $(\alpha^0 = 0.98)$. The function $\psi(\alpha)$ refers to the cure dependent energy barrier related to a thermorheologically simple material, expressed as

$$\psi(\alpha) = 9.1347\alpha^2 + 0.6089\alpha - 9.3694 \tag{2.50}$$

Finally, λ_i refers to a spectral response that describes the distribution of the time relaxation scales as follows

$$\lambda_i = \frac{10^{9.9}}{\tau_i(\alpha^0)} \tag{2.51}$$

Then, the relaxation modulus for the Generalized Maxwell Model in an incremental strain material, presented in *(2.40)* becomes

$$G(\alpha, T, \xi^t - \xi') = Q_0 + \sum_{i=1}^{N} Q_i e^{\left(\frac{\xi^t - \xi'}{\tau_i(\alpha)\cdot\theta_T(\alpha,T)}\right)} \tag{2.52}$$

This equation describes isotropic viscous materials. Therefore, authors have changed the above equation to apply to the laminate composite material. The stiffness matrix for laminate composite can be expressed as

$$Q_{ij}(\alpha,\xi) = Q_{ij}^{\infty} + (Q_{ij}^{u} - Q_{ij}^{\infty}) \sum_{m=1}^{N} W_m \exp\left(-\frac{\xi}{\tau_m(\alpha)}\right) \qquad (2.53)$$

Where Q_{ij}^{∞} indicates the fully relaxed stiffness and Q_{ij}^{u} is the unrelaxed modulus. Both moduli can be assumed to be cure-independent and related by a partition factor χ as follows [56],

$$Q_{ij}^{\infty} = \chi Q_{ij}^{u}, \;\; 0 \leq \chi \leq 1 \qquad (2.54)$$

Here, $\chi = 0$ refers to a completely relaxed composite and $\chi = 1$ means unrelaxed composites. In this work, a value of $\chi = 0.1$ was assumed, which is for AS4/3501-6 materials[56]. W_m is the weight factor for the m-th Maxwell element.

Before completing the stress-strain relation of the material. The effect of the curing shrinkage in thermosetting polymers must be taken into account.

During the polymerization, the material networks that contribute to the stiffening of the material undergo an inherent shrinkage. A model that depicts this process is presented in [57]. The contribution of the chemical shrinkage to the effective strain is given by

$$\varepsilon_{cs} = \phi_{cs} \Delta\alpha \qquad (2.55)$$

Where ϕ_{cs} refers to the coefficient of chemical shrinkage. Similarly, the contribution of the material thermal expansion is

$$\varepsilon_{th} = \phi_{th}\Delta T \tag{2.56}$$

Then, the effective strain is

$$\varepsilon^{eff} = \varepsilon_{mech} - \varepsilon_{cs} - \varepsilon_{th} \tag{2.57}$$

Where ε_{mech} refers to the mechanical strain.

Then, the material constitutive relationship is rewritten as

$$\sigma_i(t) = \int_0^t G_{ij}(\alpha, T, \xi^t - \xi') \frac{\partial \varepsilon_j^{eff}}{\partial s} ds \tag{2.58}$$

2.4 Random Field Modeling

Several parameters used in modern computational models are obtained from complex experimental procedures. The random nature of these parameters increases the difficulty of predicting the final material response by utilizing traditional deterministic methods [58]. The analysis of stochastic properties requires high computational resources. However, this analysis must be considered to overcome the limitations of simpler models. Because of this, the probabilistic modeling of mechanical problems is becoming a state-of-the-art approach that is gaining

popularity in the scientific community. This section presents one of the various methods commonly used in random the field modeling.

A compelling computational tool in the probabilistic analysis of material uncertainties is the Stochastic Finite Element Method (SFEM). A review of developments in the SFEM area are listed in [59]. Where the author includes: spectral representation method, Karhunen-Loève Expansion (KLE), the turning band method and the autoregressive moving average among others. This work will focus on the KLE method.

Stochastic parameters can be modeled as random variables or random fields [60]. KLE method is a continuous random field representation that comprises orthogonal deterministic functions. The formulation of the orthogonal series expansion presented in the following section is obtained from [60].

2.4.1 Orthogonal Series Expansion

Considering a random field function $R(x)$, where x represents a position vector indexed on a physical domain Ω. The determinist and stochastic parts of this function can be presented as a Fourier-type series

$$R(x) = \bar{R} + \sum_{i=1}^{\infty} c_i \nu_i \varphi_i(x) \tag{2.59}$$

Here, $\bar{R}$ is the mean value, which will be considered as constant in this work [61]. $\varphi_i(x)$ refers to a set of statistically uncorrelated random variables (orthonormal deterministic functions); c_i and ν_i constant coefficients and random variables respectively. The covariance function is written as follows

$$C(x_1; x_2) = E[(R(x_1) - \bar{R}) \cdot (R(x_2) - \bar{R})] \tag{2.60}$$

Where $E[\,]$ refers to the mathematical expectation. Then, substituting (2.59) in (2.60) yields to

$$C(x_1; x_2) = \sum_{i=1}^{\infty} \sum_{j=1}^{\infty} c_i c_j E\left[\nu_i \nu_j\right] \varphi_i(x_1) \varphi_j(x_2) \tag{2.61}$$

If (2.75) is multiplied by $\varphi_k(x_1)$, and integrated over the domain Ω with respect to x_1, the following equation is obtained

$$\int_{\Omega} C(x_1; x_2)\, \varphi_k(x_1) dx_1 = \sum_{j=1}^{\infty} c_k c_j E\left[\nu_k \nu_j\right] \varphi_j(x_2) \tag{2.62}$$

The same way, the multiplication of (2.76) by $\varphi_l(x_2)$ and integration over Ω with respect to x_2 results in

$$\int_{\Omega} \int_{\Omega} C(x_1; x_2) \varphi_k(x_1) \varphi_l(x_2) dx_1 dx_2 = c_k c_l E[\nu_k \nu_l] \tag{2.63}$$

This equation can be rewritten as

$$c_k c_l E[\nu_k \nu_l] = \int_\Omega C(x_1; x_2)\varphi_k(x_1)dx_1 \int_\Omega \varphi_l(x_2)dx_2 \quad (2.64)$$

The KLE can be considered as a variation of the orthogonal series expansion presented. This method is detailed in the following section.

2.4.2 Karhunen-Loève Expansion

In KLE, the square of the constant coefficient c_i^2 and the orthonormal function $\varphi_i(x)$ are the eigenvalue λ_i and eigenfunction $f_i(x)$ of the autocovariance function $C(x_1, x_2)$ respectively. Hence, (2.59) becomes

$$R(x) = \bar{R} + \sum_{i=1}^{\infty} \sqrt{\lambda_i}\nu_i f_i(x) \quad (2.65)$$

Here, (2.64) can be expressed as

$$\sqrt{\lambda_k}\sqrt{\lambda_l}E[\nu_k \nu_l] = \int_\Omega f_l(x_2)f_k(x_2)\lambda_k dx_2 \quad (2.66)$$

Where

$$\int_\Omega f_l(x_2)f_k(x_2)\lambda_k dx_2 = \lambda_k \delta_{lk} \quad (2.67)$$

Here, δ_{lk} is the Kronecker delta. Consequently, from (2.66) and (2.67) the following relation can be obtained

$$E[\nu_k \nu_l] = \delta_{lk} \quad (2.68)$$

This shows that the random variables are statistically uncorrelated.

The discretization of the random field $R(x)$ is obtained from truncating the series in (2.65) at a value K. [62]

$$R(x) = \bar{R} + \sum_{i=1}^{K} \sqrt{\lambda_i} \nu_i f_i(x) \tag{2.69}$$

The covariance function presents the spectral decomposition. This because, by definition, it is bounded, symmetric and positive definite [63]. Then, by considering the relation in (2.68), the covariance shown in (2.61) becomes

$$C(x_1; x_2) = \sum_{i=1}^{K} \lambda_i f_i(x_1) f_i(x_2) \tag{2.70}$$

Where the eigenvalue and eigenfunction are the solution of the Fredholm equation of the second kind

$$\int_{\Omega} C(x_1; x_2) f_i(x) dx_1 = \lambda_i f_i(x_2) \tag{2.71}$$

The covariance function depends on the random field characteristics. A typical exponential form for a 2-dimension domain is provided in [61]

$$C(x_1; x_2) = \sigma^2 exp\left(\frac{|x_1 - x_2|}{b_1 L_1} - \frac{|y_1 - y_2|}{b_2 L_2}\right) \tag{2.72}$$

Here, b_i and L_i are the correlation length parameters and physical characteristic lengths in each direction respectively. The standard

deviation is represented by σ. The correlation length is obtained from the following equation

$$L_{ci} = biLi \tag{2.73}$$

The main setback in the implementation of the KLE is the difficulty to obtain analytical solutions for the integral equation (2.71). Especially when the domain Ω has an irregular shape. This is because the analytical solutions are limited to simple geometries and special forms of the auto covariance function [59]. A way to overcome this is by utilizing a Galerkin finite element approach [61]. The stochastic finite element method can be implemented with a Monte Carlo simulation.

2.4.3 Parameters to be randomized

The cure kinetics play an important role in the modeling of the material behavior, involving both: the thermochemical and mechanical analysis. Some authors have presented the notion of networks that contribute to the stiffening of the material during the curing process [57]. The stochastic behavior related to the random distribution of these networks can be produced by randomizing the parameters from the Arrhenius equation presented in (2.3). These parameters are commonly obtained from curve fitting procedures and considered as constants over the entire

domain despite of their random nature. Since the frequency factors A_i and the energy activation parameters ΔE_i are strongly related to each other [37], it is enough to randomize just one of them. The parameters selected to be randomized are the frequency factors A_i.

2.5 Classical Lamination Theory

Classical lamination theory (CLT) is used to calculate macroscopic residual stresses of thin composite laminates. Different ply orientations lead to combinations of flexural and torsional deformations. This model considers extensional (A_{ij}), coupling (B_{ij}) and bending stiffness (D_{ij}) matrices presented in the following equations[2].

$$A_{ij} = \sum_{k=1}^{N} \bar{Q}_{ij}^{k} (z_k - z_{k-1}) \tag{2.74}$$

$$B_{ij} = \frac{1}{2} \sum_{k=1}^{N} \bar{Q}_{ij}^{k} (z_k^2 - z_{k-1}^2) \tag{2.75}$$

$$D_{ij} = \frac{1}{3} \sum_{k=1}^{N} \bar{Q}_{ij}^{k} (z_k^3 - z_{k-1}^3) \tag{2.76}$$

Here, $\bar{Q}_{ij}$ refers to the stiffness matrix index and z_k is the interlaminar height of the kth lamina. The stress-strain relation can be expressed as

$$\begin{Bmatrix} N \\ M \end{Bmatrix} = \begin{bmatrix} A & B \\ B & D \end{bmatrix} \begin{Bmatrix} \varepsilon^0 \\ \kappa \end{Bmatrix} \tag{2.77}$$

Where N and M are the force per unit length and the moment per unit length respectively. The strain at the midplane is ε^0 and the lamina bending curvature is κ.

Due to the thermal properties of each lamina, the plates are subjected to tension and compression forces during the cool down and post curing stages. The calculation of the thermal loads is [24]

$$(N_x^T; M_x^T) = \sum_{k=1}^{N} \left[\bar{Q}_{11}^k \alpha_x^k + \bar{Q}_{12}^k \alpha_y^k + \bar{Q}_{16}^k \alpha_{xy}^k\right] \Delta T_k \cdot (t_k, t_k \bar{z}_k) \tag{2.78}$$

$$\left(N_y^T; M_y^T\right) = \sum_{k=1}^{N} \left[\bar{Q}_{21}^k \alpha_x^k + \bar{Q}_{22}^k \alpha_y^k + \bar{Q}_{26}^k \alpha_{xy}^k\right] \Delta T_k \cdot (t_k, t_k \bar{z}_k) \tag{2.79}$$

$$\left(N_{xy}^T; M_{xy}^T\right) = \sum_{k=1}^{N} \left[\bar{Q}_{61}^k \alpha_x^k + \bar{Q}_{62}^k \alpha_y^k + \bar{Q}_{66}^k \alpha_{xy}^k\right] \Delta T_k \cdot (t_k, t_k \bar{z}_k) \tag{2.80}$$

Here, α_i^k and ΔT_k are the thermal expansion coefficient and the difference between the stress-free and the ambient temperature respectively. The ply thickness is t_k and the lamina midplane height is $\bar{z}_k$. The midplane strain and curvature are:

$$\varepsilon^0 = \alpha \cdot \left(N_x^T, N_y^T, N_{xy}^T\right) + \beta \cdot \left(M_x^T, M_y^T, M_{xy}^T\right) \tag{2.81}$$

$$\kappa^0 = \beta^T \cdot \left(N_x^T, N_y^T, N_{xy}^T\right) + \gamma \cdot \left(M_x^T, M_y^T, M_{xy}^T\right) \tag{2.82}$$

The matrices α, β and γ are calculated as follows:

$$\alpha = \boldsymbol{A}^{-1}\boldsymbol{B}\boldsymbol{D}^{*-1}\boldsymbol{D}\boldsymbol{B} \tag{2.83}$$

$$\beta = -\boldsymbol{A}^{-1}\boldsymbol{B}\boldsymbol{D}^{*-1} \tag{2.84}$$

$$\gamma = \boldsymbol{D}^{*-1} \tag{2.85}$$

$$\boldsymbol{D}^{*} = \boldsymbol{D} - \boldsymbol{B}\boldsymbol{A}^{-1}\boldsymbol{B} \tag{2.86}$$

Finally, the interlaminar residual stress and strain are given by:

$$\varepsilon^{k} = \varepsilon^{0} + \bar{z}_{k}\,\kappa^{0} - \alpha^{k}\Delta T \tag{2.87}$$

$$\sigma^{k} = \bar{Q}_{ij}^{k}\varepsilon^{k} \tag{2.88}$$

Chapter 3. Materials and Methodology

3.1 Materials

In this work, 3501-6 epoxy/Hexcel AS4 composite laminates of 300mm x 300mm x 3mm were modeled to obtain the interlaminar stress development during the manufacturing process. The selection of this material responds to the information available in the literature that makes possible the virtual modeling of the laminates. The mechanical and thermal properties of the resin and the fibers are shown in Table 3.1 and Table 3.2, respectively [26]. The material unrelaxed properties are shown in Table 3.3 [25]

Table 3.1.Resin properties

Parameter	Value	Unit
ρ_m	$90\alpha + 1232\ (\alpha \leq 0.45)$ $1272\ (\alpha > 0.45)$	kg/m^3
C_m	$4184\ \times\ (0.468 + 5.975 \times 10^{-4}\,T - 0.141\ \alpha)$	$J/(kg\ K)$
λ_m	$0.04184\ \times\ (3.85 + (0.035\ T - 0.141\ \alpha)$	$W/(m\ K)$
H_m	47.36×10^{-4}	J/kg
R	8.3143	$J/(mol\ K)$
A_1	35.017×10^6	$1/s$
A_2	-33.567×10^6	$1/s$
A_3	3266.67	$1/s$
ΔE_1	8.07×10^4	J/mol
ΔE_2	7.78×10^4	J/mol
ΔE_3	5.66×10^4	J/mol

Table 3.2.Fiber properties

Parameter	Value	Unit
ρ_f	1790	kg/m^3
C_f	$750 + 2.05\ T$ (℃)	$J/(kg\ K)$
λ_f^L	$7.69 + 0.0156\ T$ (℃)	$W/(m\ K)$
λ_f^T	$2.4 + 0.00507\ T$ (℃)	$W/(m\ K)$

Table 3.3. Unrelaxed properties on the principal directions

Parameter	Value	Unit
$\nu_{12} = \nu_{13}$	0.25	−
$\nu_{23} = \nu_{32}$	0.53	−
$\nu_{31} = \nu_{21}$	0.0165	−
E_1	126.0	GPa
$E_2 = E_3$	8.3	GPa
$G_{12} = G_{13}$	4.1	GPa
G_{23}	2.8	GPa
CTE_1	0.5	$\mu\varepsilon$/℃

$CTE_2 = CTE_3$	35.3	$\mu\varepsilon/℃$
CCS_1	-167	$\mu\varepsilon$
$CCS_2 = CCS_3$	$-8\,810$	$\mu\varepsilon$

Here, each lamina can be considered as an especially orthotropic and transversely isotropic material. Since the fiber dominated directions of the laminate produce a linear elastic response, the viscoelastic behavior is limited to Q_{22}, Q_{33}, Q_{44}, Q_{55}, Q_{66}, Q_{23} and Q_{32}. The parameters that build the unrelaxed stiffness matrix Q_{ij} are given by

$$
\begin{aligned}
Q_{11} &= \frac{1-\nu_{23}\nu_{32}}{\nabla}E_1 \\
Q_{12} &= \frac{\nu_{21}+\nu_{31}\nu_{23}}{\nabla}E_1 \\
Q_{13} &= \frac{\nu_{31}+\nu_{21}\nu_{23}}{\nabla}E_1 \\
Q_{23} &= \frac{\nu_{32}+\nu_{12}\nu_{31}}{\nabla}E_2 \\
Q_{22} &= \frac{1-\nu_{13}\nu_{31}}{\nabla}E_2 \\
Q_{44} &= G_{23} \\
Q_{55} &= G_{13} \\
Q_{66} &= G_{12} \\
\nabla &= 1-\nu_{12}\nu_{21}-\nu_{23}\nu_{32}-\nu_{31}\nu_{13}-2\nu_{21}\nu_{32}\nu_{13}
\end{aligned}
\tag{3.1}
$$

Here, the weight factors and the stress relaxation time used in the Generalized Maxwell Model for AS4/3501-6 composites are summarized in Table 3.4 [56].

Table 3.4. Weight factors and stress relaxation time

ω	$\tau_\omega(min)$	W_ω
1	2.92×10^1	0.059
2	2.92×10^3	0.066
3	1.82×10^5	0.083
4	1.10×10^7	0.112
5	2.83×10^8	0.154
6	7.94×10^9	0.262
7	1.95×10^{11}	0.184
8	3.32×10^{12}	0.049
9	4.92×10^{14}	0.025

The viscoelastic model used considers cure dependent properties, the formulation of this dependency is given in Chapter 2. The stochastic finite element analysis used in this thesis is based on the work of Shang, S. and Yun, G.J. [61]. Here, the Monte Carlo simulation is used to produce the behavior of the random parameters of frequency factors A_i. In addition, anisotropic correlation lengths were included as in the work of Zhu, Fei-Yan [64]. The values of the correlation lengths (L_{ci}), mean value and covariance used in this work are given in Table 3.5.

Table 3.5. KLE parameters

Parameter	Mean	COV	L_{C1}	L_{C2}	L_{C3}
A_1	2.101	0.25	0.002	0.002	0.001
A_2	2.014	0.25	0.002	0.002	0.001
A_3	1.960	0.25	0.002	0.002	0.001
E_2	8.300	0.25	0.002	0.002	0.001
G_{12}	4.100	0.25	0.002	0.002	0.001
G_{23}	2.800	0.25	0.002	0.002	0.001

The truncation value K is set to 2061 for all cases. The values obtained for A_1, A_2 and A_3 are then multiplied by the factors $1e^9$, $-1e^9$ and $1e^5$ respectively.

3.2 Methodology

A total of six plates with different layup configurations as shown in Table 3.6 were modeled to analyze the relation between ply orientation, residual stress, and deformation.

Table 3.6. Layup Configuration

Name	Layup Configuration	Type
Plate P1	$[90_3/0_3]$	Asymmetric Cross-Ply
Plate P2	$[(90/0)_3]$	Asymmetric Cross-Ply
Plate P3	$[90_2/0]_s$	Symmetric Cross-Ply
Plate P4	$[45_2/0]_s$	Symmetric Angle-Ply
Plate P5	$[(30/-30)_3]$	Antisymmetric Angle-Ply
Plate P6	$[-60/-30/0/30/60/90]$	Quasi Isotropic Laminate

Due to geometric symmetry, only a quarter of the plate was modeled as shown in Figure 3.1. Here, Edges X0, Y0, and XY refer to the areas of

interest, where the stress and displacement information is taken from five interlaminar nodes, labeled in Figure 3.2.

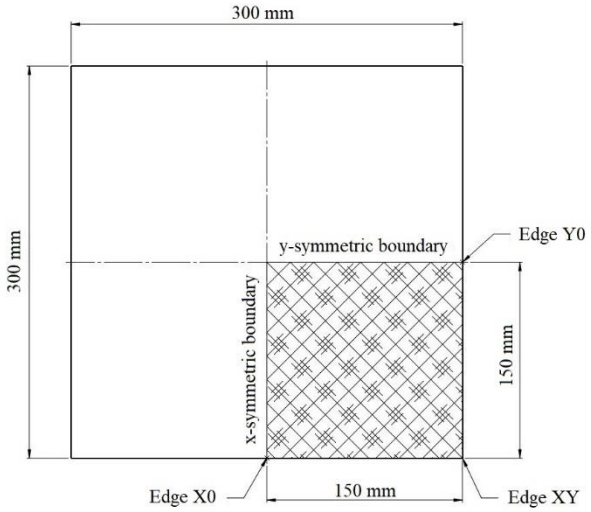

Figure 3.1. Laminate geometry

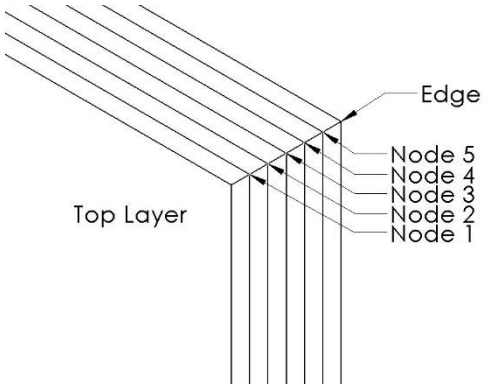

Figure 3.2. Analyzed Nodes

The process is divided into four sections:

- **Section 1:** Curing stage. This section refers to the Vacuum Assisted Resin Transfer Molding (VARTM) process presented in Figure 3.4. Here, the plate is inside a rigid mold, which means that the mechanical boundary conditions for all of the surfaces (except for the planes of symmetry) are constrained. Also, the plate is subjected to the temperature of the curing process. Thermal conduction from the mold to the upper and lower surfaces of the plate was simulated.
- **Section 2:** Cool down. At this stage, the completely cured plate is removed from the mold. Here, the symmetry boundary conditions are the same as in the previous step. However, the constraining boundary conditions are eliminated. Thus, free boundary conditions are applied. The edge along z at $x = y = 0$ is considered as the center of the plate, which is pinned to avoid displacement in the z direction and to be used as the reference. For the thermal boundary conditions, it is important to note that the plate is now free from the mold and exposed to room temperature. Therefore, natural free convection was simulated considering a film coefficient of $3.5\ \mathrm{W}/m^2K$ and a sink temperature of $298\ K$.

- **Section 3:** Rising the temperature to an Isothermal. At this stage, the cooled plate is placed into an oven with an isothermal of $400\ K$. The mechanical boundary conditions are the same as in the previous step. The thermal boundary conditions are also similar with the difference that now the plates are under forced convection, so, the new film coefficient is $30\ \mathrm{W}/m^2K$ and the sink temperature is $400\ K$.
- **Section 4:** Final Cool down. This is the last stage of the process simulation. The mechanical and thermal boundary conditions are the same as in Section 2.

The temperature cycle during the manufacturing process is shown in Figure 3.3.

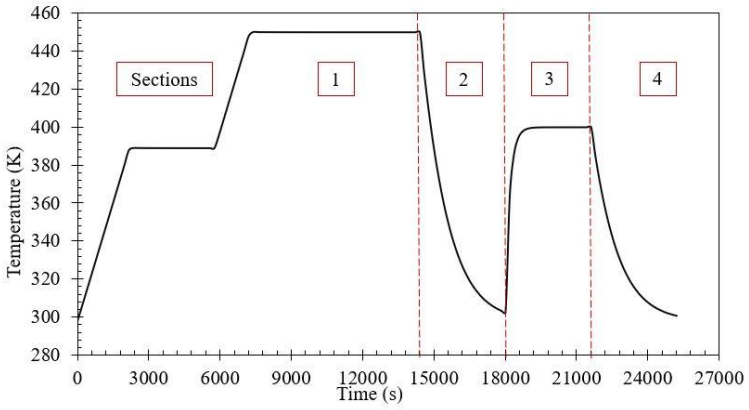

Figure 3.3. Temperature profile

3.3 Experimental Setup

Two representative plates were manufactured. It is important to mention that the epoxy used in the computational analysis was not available. Because of this a different epoxy was used. Nevertheless, since both resins are thermosetting materials that undergo similar shrinkage processes, it is possible to observe the final shape of the deformed plates after the curing stage (sections 1 and 2) and conduct a quantitative comparison with the computational model.

In this case, the resin is a Kinetix R118 epoxy mixed with Kinetix H126 hardener at a ratio of 25 parts of hardener to 100 parts of resin. The curing cycle was performed following the manufacturer recommendation. The Vacuum Assisted Transfer Molding schematics used in this experiment and photo of the actual equipment is shown in Figure 3.4 and Figure 3.5 respectively.

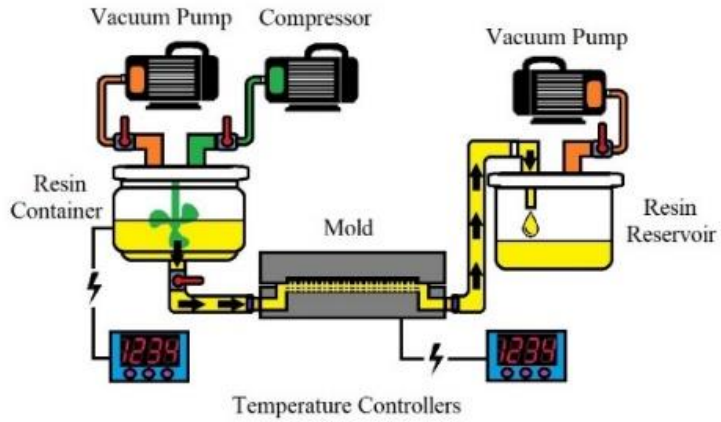

Figure 3.4. VARTM schematics

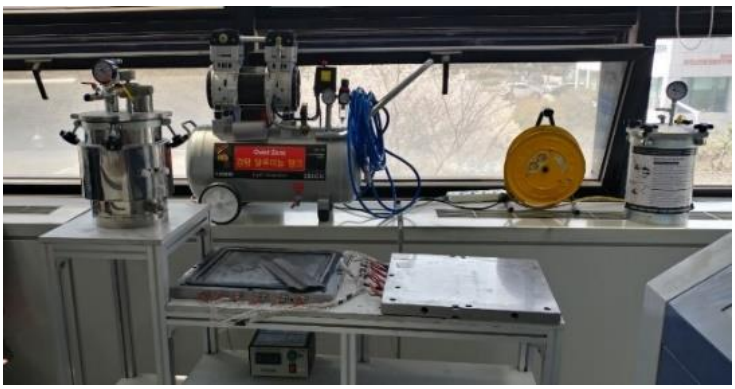

Figure 3.5. Actual RTM setup

The plate deformations were measured using a Sense 3D Scanner from the company 3D Systems. This equipment has a x/y spatial resolution of 0.9 mm and a depth resolution of 1 mm.

Chapter 4. Model Verification

To verify the model proposed in this work, a laminate composed of four layers symmetric about the x-y plane was created as in the literature[65]. This symmetric cross-ply laminate $[0/90]_s$ has dimensions of 101.6 mm each side and a thickness of 25.4 mm. To efficiently use the computational resources, a quarter of the plate is modeled. The boundary conditions are applied considering the geometric symmetry of the laminate. The FE model is presented in Figure 4.1. Here, the normal interlaminar stress (σ_{33}) is obtained from Node X0, located at $x = z = 0$ and $y = 50.8\,mm$. While the normal strain (ε_{33}) is obtained from the center of the laminate ($x = y = z = 0$). The results of Node X0 are compared with the work of White and Kim [65] and the results obtained from the laminate center are compared with the work of Yuan et al.[26].

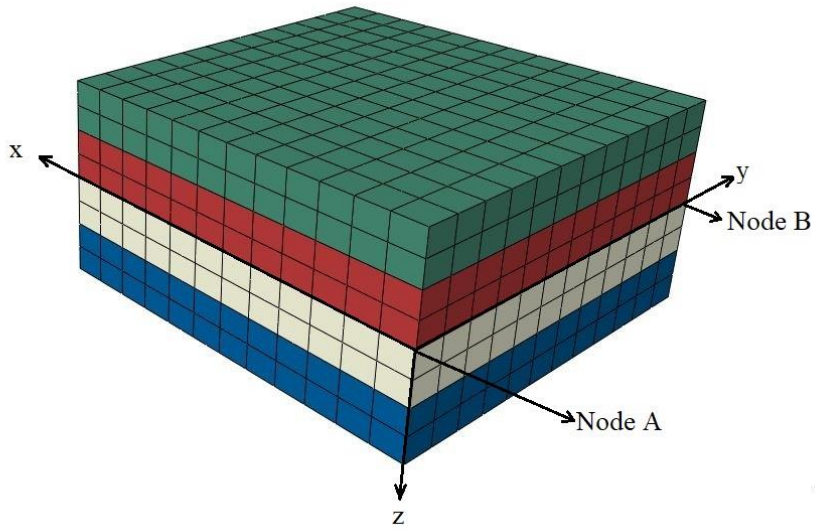

Figure 4.1. FE model for laminate

The mechanical boundary conditions are free, and the planes of symmetry are located at $x = 0$ and $y = 0$. For the thermal boundary conditions, the plate is subjected to a heat transfer over the top and bottom layers. Here, the temperature rises from 298 K to 389 K at a constant rate of 2.5 K/min. This temperature remains constant for 60 minutes and then increases to the second dwell temperature of 450 K at a rate of 2.5 K/min. After 120 minutes, the temperature decreases to room temperature at a constant rate of -2.5 K/min. The temperature and degree of cure history of the AS4/3501-6 laminate is shown in Figure 4.2.

The material properties and boundary conditions are the same as in the references.

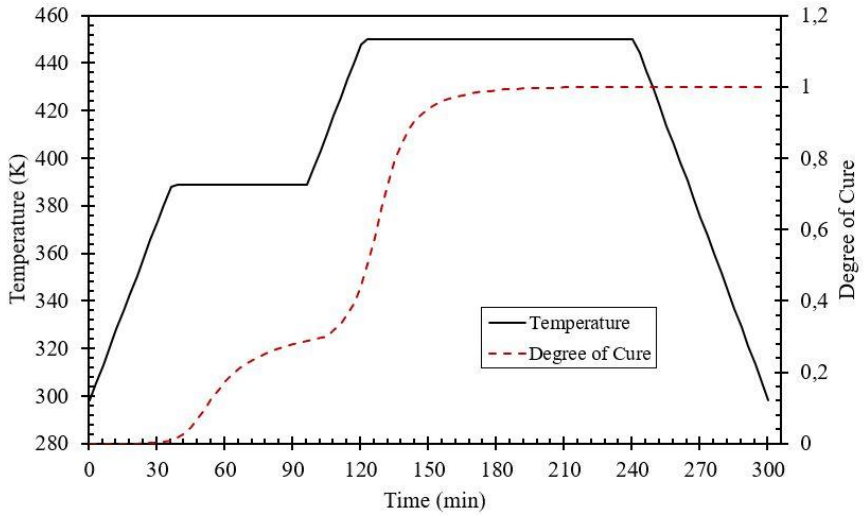

Figure 4.2. Temperature and degree of cure history

The calculated interlaminar normal stress (σ_{33}) is shown in Figure 4.3 and the strain in the z-direction (ε_{33}) is shown in Figure 4.4. The accuracy of the results verifies the proposed model.

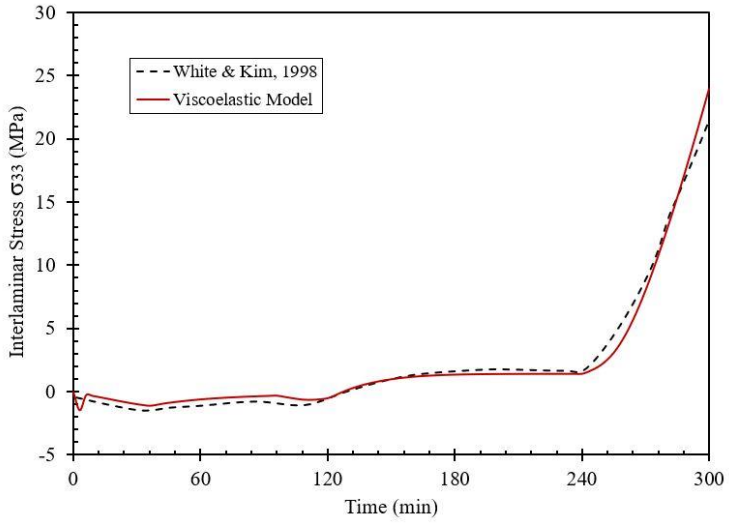

Figure 4.3. Normal Interlaminar Stress at Node B

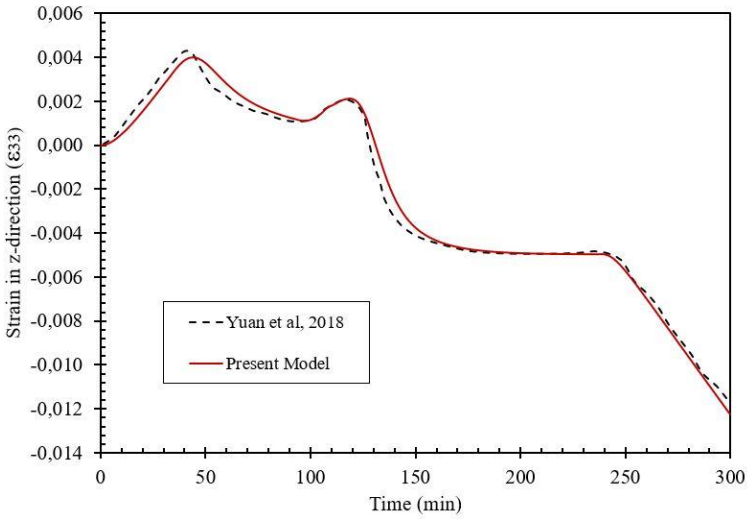

Figure 4.4. Normal Strain at Node A

Chapter 5. Results

5.1 Residual stress comparison

Plates P1 and P2 have an asymmetric cross-ply layup configuration of $[90_3/0_3]$ and $[(90/0)_3]$, respectively. The interlaminar residual stress buildup during the curing process (Step 1) for all the analyzed nodes is identical in both cases as shown in Figure 5.1. Here, the continuous line represents the total stress (including thermal expansion and chemical contraction). A dotted line is added as a reference. This dotted line represents a hypothetical case in which the chemical shrinkage is neglected and only the thermal expansion is considered. The maximum stress in both plates is obtained at the end of the step, with a magnitude of 35.54 MPa.

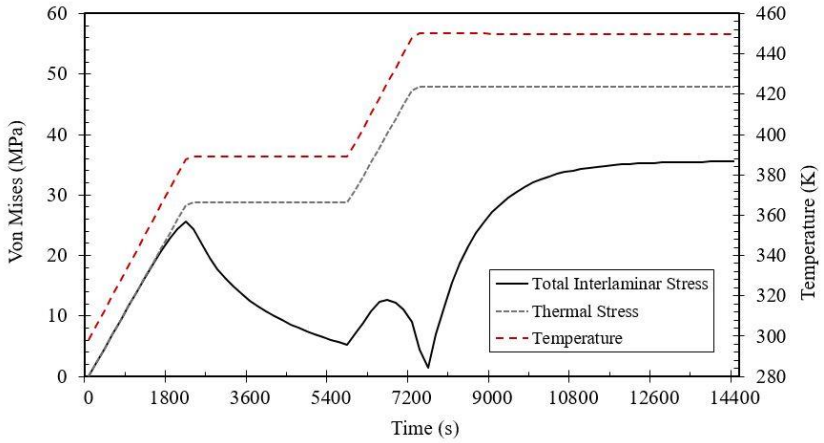

Figure 5.1 Cure Cycle Interlaminar Stress (Plates P1, P2, and P3)

The plates are mechanically constrained in the mold until they reach the crystallization point. Once this stage ends, they are released from the mold and left to cool down by natural free convection (Section 2). At this point, the plates undergo residual distortions.

Plates P3 and P4 have symmetric cross-ply $[90_2/0]_s$ and symmetric angle-ply $[45_2/0]_s$ configuration, respectively. The residual stress buildup during Step 1 for plate P3 is the same as in plates P1 and P2. However, in Plate P4, the stress distribution differs in each interlaminar node. The higher values are observed in Edge XY, these are shown in Figure 5.2, where the maximum stress is observed at Node 4 (119.20 MPa).

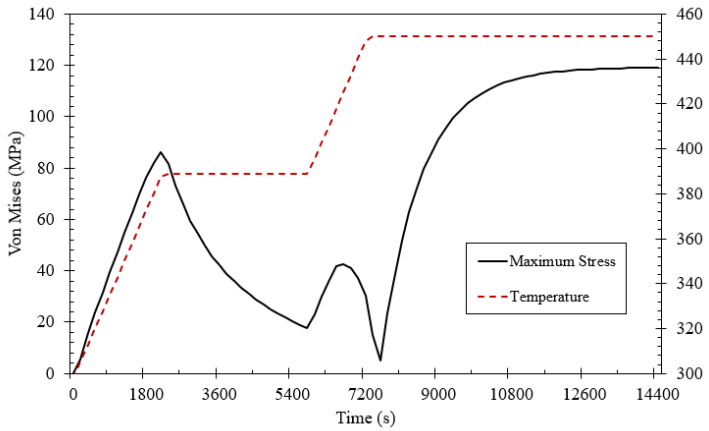

Figure 5.2. Cure Cycle Maximum Stress (Plate P4)

Plate P5 has an antisymmetric angle-ply layup configuration $[(30/-30)_3]$. Figure 5.3 shows the curing stage interlaminar stress buildup in Edge XY. The maximum stress (41.45 MPa) is observed at Node 1.

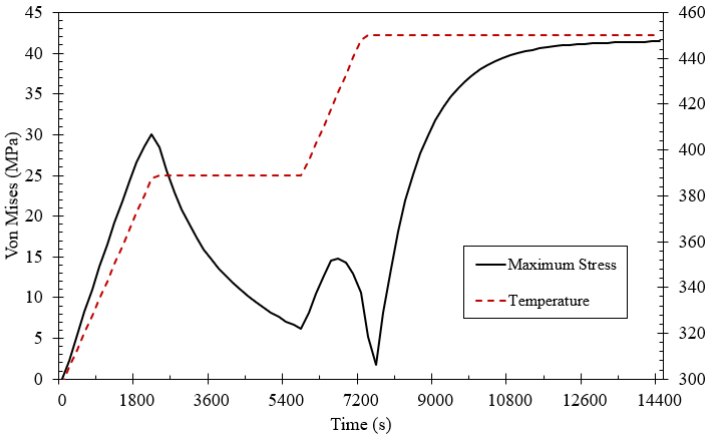

Figure 5.3. Cure Cycle Maximum Stress (Plate P5)

Finally, the quasi-isotropic laminate is plate P6 with a ply orientation of $[-60/-30/0/30/60/90]$. This plate shows the higher values of interlaminar stress among all the laminate configurations studied during Section 1. The maximum residual stress is observed at Node 5 in Edge Y0 (48.79 MPa) as shown in Figure 5.4

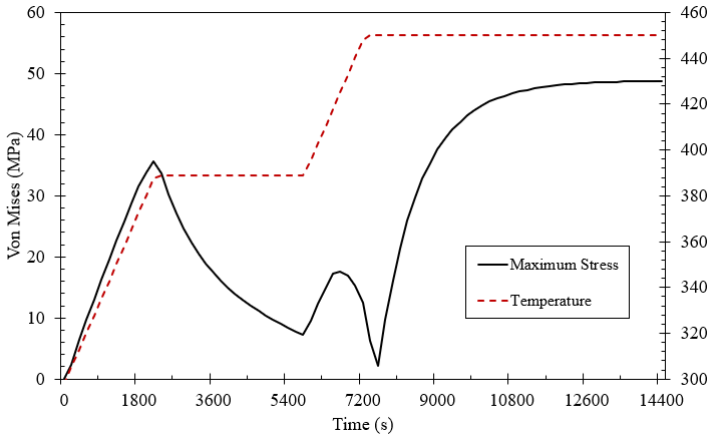

Figure 5.4. Cure Cycle Maximum Stress (Plate P6)

5.2 Cure-induced distortion

The cured-induced distortions were obtained at the cool down stage (Section 2). Here the plates are released from the mold and cooled down to room temperature (298 K). The distorted plates P1 and P2 are identical in shape, but the magnitude of the displacements differs. Figure 5.5 shows the deformed Plate P1 at the end of this section. The maximum

displacement in Plates P1 and P2 are 12.19 mm and 1.70 mm, respectively.

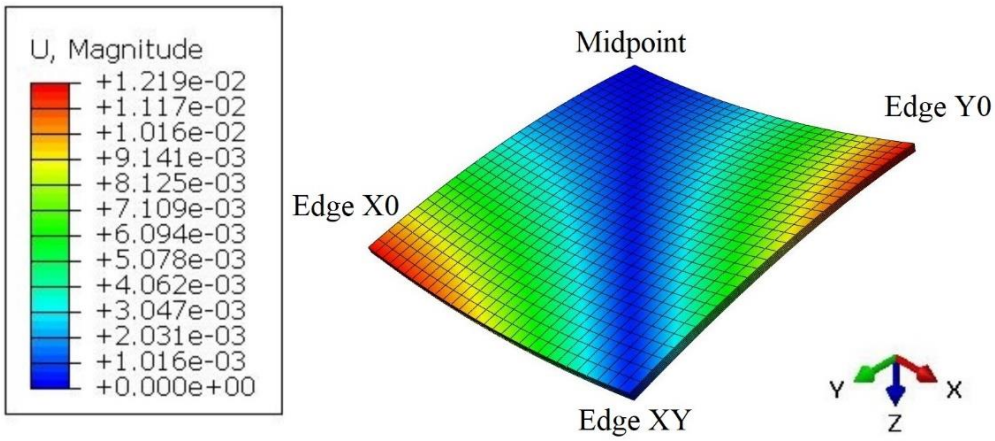

Figure 5.5. Deformed Plate P1 after cool down

The cooldown distortions of laminates P3 and P4 are similar. In both cases the plate contracts over the in-plane directions without twisting or bending. Figure 5.6 and Figure 5.7 show the displacement in the x-direction of both plates to illustrate the difference of the displacement distribution. The maximum nodal displacements in plates P3 and P4 are 0.12 mm and 0.74 mm, respectively.

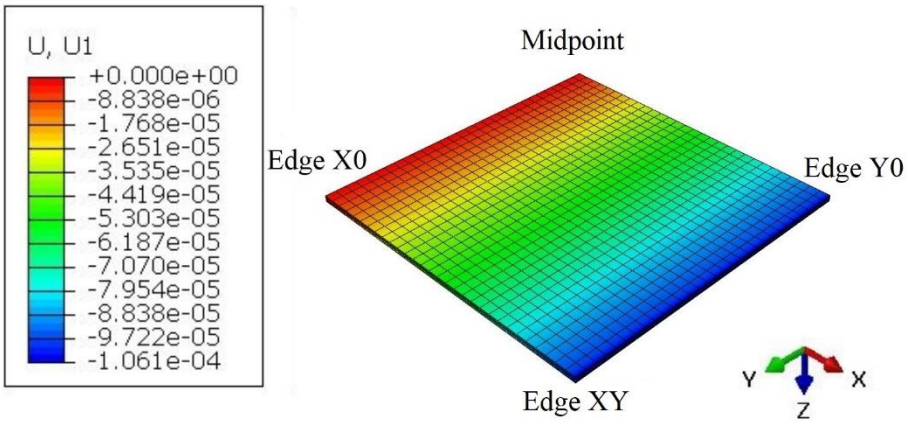

Figure 5.6. Cool down displacement in the x-direction (Plate P3)

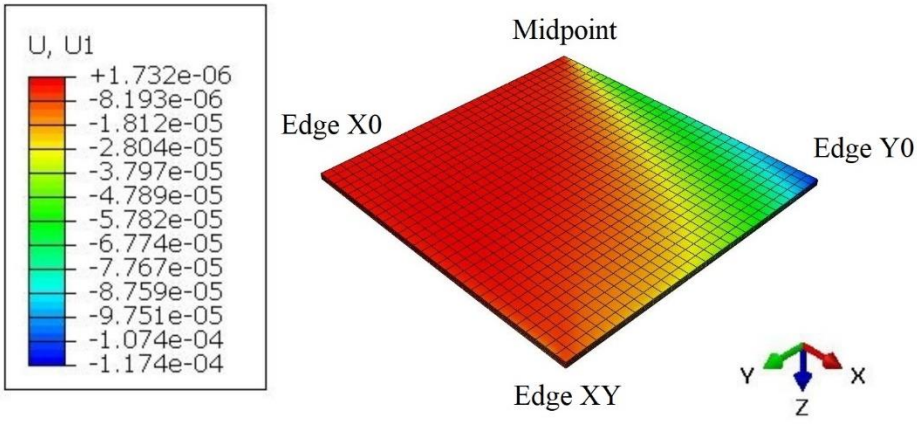

Figure 5.7. Cool down displacement in x-direction (Plate P4)

The deformation of the antisymmetric angle-ply plate P5 is shown in Figure 5.8.

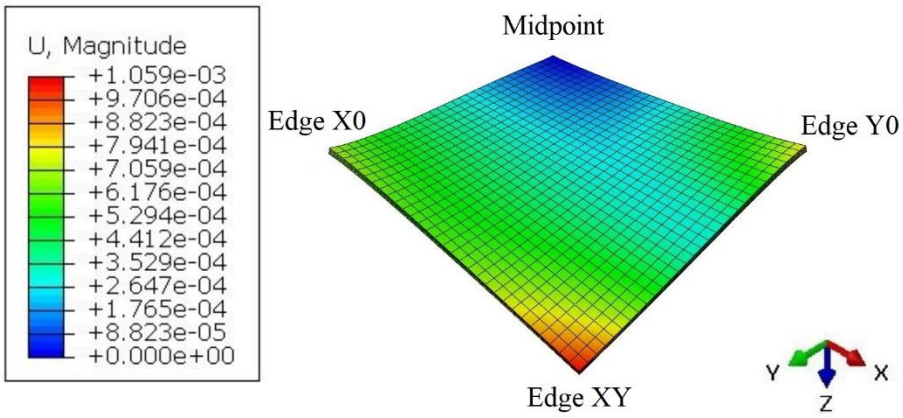

Figure 5.8. Deformed Plate P5 after cool down

The distortion of Plate P6 is shown in Figure 5.9. Here, the maximum distortion location is evidently in Edge Y0. The displacement magnitude of 14.06 mm is the highest value observed on all the laminates.

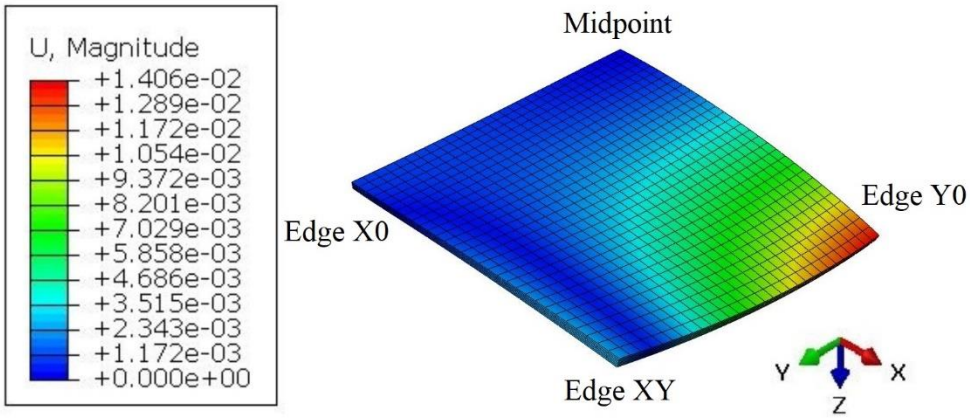

Figure 5.9. Deformed Plate P6 after cool down

A summary of the maximum absolute displacement in each main direction at the end of the cool-down stage over edges X0, Y0 and XY

are presented in Figure 5.10, Figure 5.11 and Figure 5.12, respectively. The largest values are observed in laminates P1 and P6. The normal displacement (U3) is much higher than the in-plane displacements (U1 and U2). The normal displacements (U3) at laminate are shown in Figure 5.13.

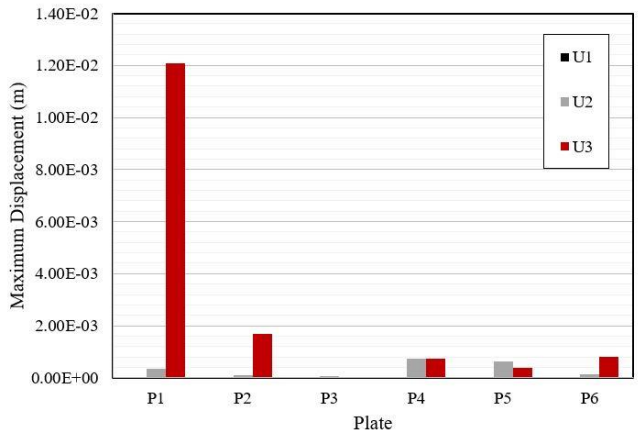

Figure 5.10. Maximum displacement in each laminate (Edge X0)

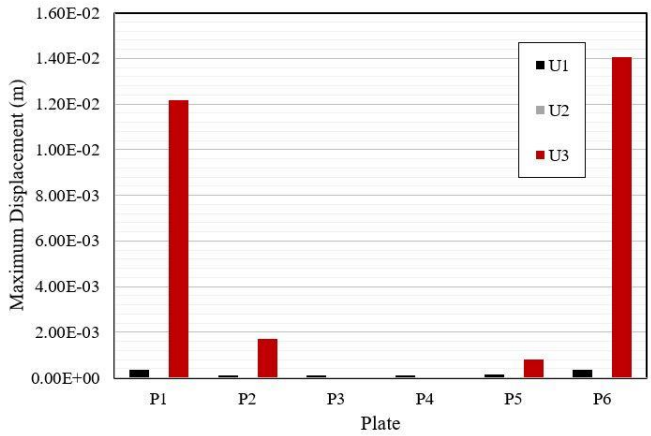

Figure 5.11. Maximum displacement in each laminate (Edge Y0)

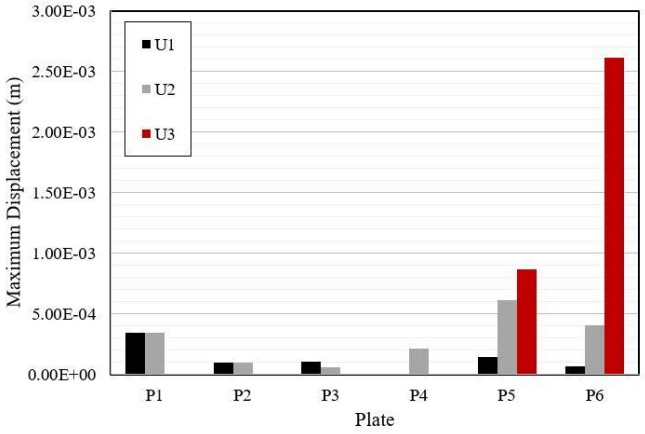

Figure 5.12. Maximum displacement in each laminate (Edge XY)

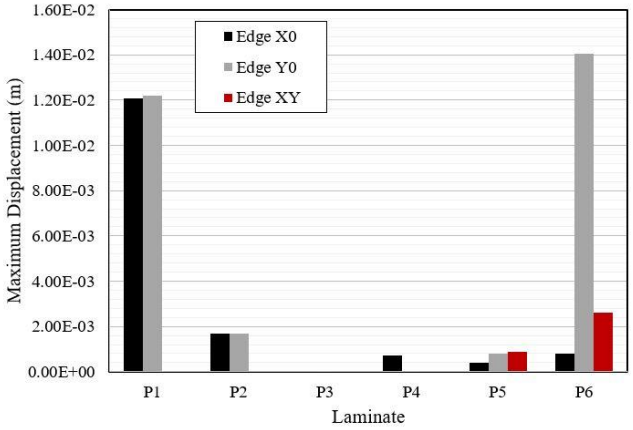

Figure 5.13. Normal displacement (U3) in each laminate

5.3 Curing-induced distortions coupling effects

A summary of the stress buildup and displacement at specific times of the curing process is made. Figure 5.14 shows the location of the steps

listed in Table 5.1. The stress and displacement results are presented in Table 5.2 and Table 5.3, respectively

Table 5.1. Step times

Step	Description	Time (s)
1	Start of the first dwell temperature	2,160
2	End of the first dwell temperature	5,760
3	Second cure shrinkage peak	6,660
4	Start of the second dwell temperature	7,200
5	End of the second dwell temperature	14,400
6	End of cool down	18,000
7	End of post-curing	25,200

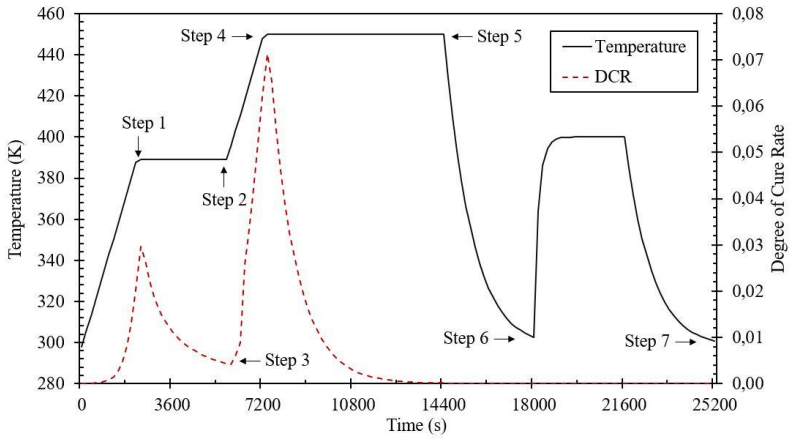

Figure 5.14. Steps for the stress analysis

Table 5.2. Maximum interlaminar stress in MPa at each laminate

Plate	P1	P2	P3	P4	P5	P6
Step 1	25.68	25.68	25.68	86.22	30.06	35.57
Step 2	5.26	5.26	5.26	17.64	6.15	7.28
Step 3	12.63	12.63	12.63	42.42	14.79	17.50
Step 4	9.05	9.05	9.05	30.34	10.58	12.51
Step 5	35.55	35.55	35.55	119.19	41.44	48.79
Step 6	39.61	32.99	48.17	72.66	24.27	42.90
Step 7	62.13	54.26	72.10	30.16	40.50	67.58

Table 5.3. Maximum displacement in mm at steps 6 and 7

Plate	P1	P2	P3	P4	P5	P6
Step 6	12.19	1.70	0.120	0.736	0.864	14.06
Step 7	12.67	1.75	0.136	0.804	0.936	14.73

The stiffness matrix of the AS4/3501-6 carbon epoxy laminate was obtained from the literature [2] and used to compute CLT matrices shown in Appendix A. The information for plates P1 and P2 is presented from Eq. (A2) to Eq. (A7). Here, the extensional matrix [**A**] and the bending matrix [**D**] of both laminates are identical; however, the bending-extension coupling matrix [**B**] shows a much lower magnitude in plate P2. This means that plate P2 will undergo smaller extensional displacements due to the bending of the laminate along x and y directions. The values for A_{16}, A_{26}, D_{16}, and D_{26} are equal to zero because of lamina shear uncoupling nature of cross-ply laminate (i.e., $\bar{Q}_{16} = \bar{Q}_{26} = 0$). For the same reason, B_{12}, B_{16}, B_{26} and B_{66} are also equal to zero in

both cases, hence, the twisting of both laminates is negligible. The distortion of plate P1 is shown in Figure 5.5. Since the deformation in plates P1 and P2 is similar, this figure works as a reference for both. It also explains why the normal displacement magnitude (U3) is higher over edges X0 and Y0 for both laminates, as seen in Figure 5.13.

The residual stress development in plates P1, P2, and P3 during the curing stage (From Step 1 to Step 5 in Table 5.2.) is not affected by the ply configuration. It is important to recall that the laminae that conform these plates have 90^{o} and 0^{o} orientations (cross-ply) and the only difference is the order in which they are placed. However, once the plates are released from the mold and left to cool down (Step 6), the stress values start to differ. It is noteworthy to highlight that even if Plate P1 and Plate P2 are both asymmetric laminates, the stress of the first one is higher than in the second one, the difference between both laminates is that in Plate P2 the laminae are alternated. Another interesting observation is that the stress magnitude in the symmetric plate P3 is higher than the stress magnitudes of P1 and P2. On the other hand, from Table 5.3 is noted that the maximum displacement is reduced in one order of magnitude for each ply configuration. Here the symmetric plate undergoes less distortions.

For the case of the symmetric Plate P4, the maximum interlaminar stresses from Step 1 to Step 5 show the highest values. However, this magnitude decreases during the cool down, when the plate is released from the mold.

The CLT matrices for the symmetric laminates (Plate P3 and Plate P4) are presented from Eq. (A8) to Eq. (A13). In both cases, the laminate coupling matrix [**B**] equal to zero, which means that there is no bending or twisting. This means that there is no coupling between in-plane deformation and out-of-plane deformation. This can be observed in Figure 5.6. It is important to note that the in-plane displacement distribution is different in both laminates. This can be explained by comparing the extensional matrix [**A**] and the bending matrix [**D**] of each plate. In the case of the cross-ply distribution (Plate P3) the elements A_{16}, A_{26}, D_{16} and D_{26} are equal to zero, which means that the laminate is limited to extensional strains. The opposite case is observed in Plate P4, where the elements are non-zero; thus, adding a shear strain component. If the displacement magnitudes shown from Figure 5.10 to Figure 5.13, are compared, it is noticeable that the magnitudes are very low compared to the rest of the laminate configurations, especially in Plate P3. However, Plate P4 shows interlaminar stress over edge XY that is 12 times higher

than in the other edges as shown in Table 5.2. This behavior is not observed in Plate P3, where all the nodes present the same interlaminar stress value. This shows how the presence of A_{16}, A_{26}, D_{16} and D_{26} components have an impact not only in the strain distribution but also in the residual stress development.

The residual stress in the antisymmetric angle-ply Plate P5 is slightly higher than in plates P1, P2, and P3 during the first five steps. However, this value decreases at the end. The CLT matrices for this plate shows that the terms A_{16}, A_{26}, B_{11}, B_{22}, B_{66}, B_{12}, D_{16} and D_{26} are equal to zero. This means that the laminate is under stretching and shearing of the mid surface and subjected to twisting. This is observed in Figure 5.8, where the maximum distortion is located at Edge XY, at the corner of the plate. Figure 5.13 shows the normal displacement at each edge, which is similar in each edge of this particular laminate. The displacement along y-direction (U2) is almost the same in edges X0 and XY with a magnitude of 0.61 mm. In the case of the x-direction (U3), Edges Y0 and XY are similar as well, in this case the magnitude is approximately 0.14 mm. This is a reflection of bending along the transverse direction and a twisting over the x-y plane.

Plate P6, as a quasi-isotropic laminate, shows an extensional stiffness [**A**]

that exhibits an isotropic behavior, as shown in Eq. (A17). However, all the terms in coupling [**B**] and bending [**D**] matrices are non-zero. This means that this material is subjected to bending and twisting. This can be observed in Figure 5.9. Here, the maximum displacement is found in Edge Y0. It is important to note that the highest interlaminar residual stress in this work is found over this edge at node 5 (between the 60º and 90º oriented laminae). From Figure 5.4, it is evident how the stress buildup at this node is higher than the rest. The same behavior can be noted in the displacement of this particular node, as shown in Figure 5.11 and Figure 5.13. The stress values obtained for Plate P6 show how the maximum stresses and displacements are strongly affected by the temperature and degree of cure. It is important to note that these values are concentrated in Edge Y0, while the rest of the plate shows negligible effects. This can be observed in Figure 5.9.

5.4 Post curing-induced stress and distortion

Once the plates are completely cured and cooled down to room temperature, they are subjected to a post-curing process. This process causes additional distortions to the laminates. The maximum distortions at the end of the cool down (Step 6) and after the post-curing section

(Step 7) are compared in Figure 5.15. For the asymmetric cross-ply Plates P1 and P2, the distortions after the post-curing process increase by 3.87 % (490 µm) and 3.27 % (57.2 µm), respectively. Both plates show a similar rate of distortion. The distortions in Plate P3 are low compared to the rest; however, the distortion after the post-curing process increase by 23.31 % (31.7 µm). Finally, the distortion in Plates P4, P5, and P6 increase in 8.52 % (80.4 µm), 7.70 % (93.6 µm), and 4.61 % (680 µm), respectively.

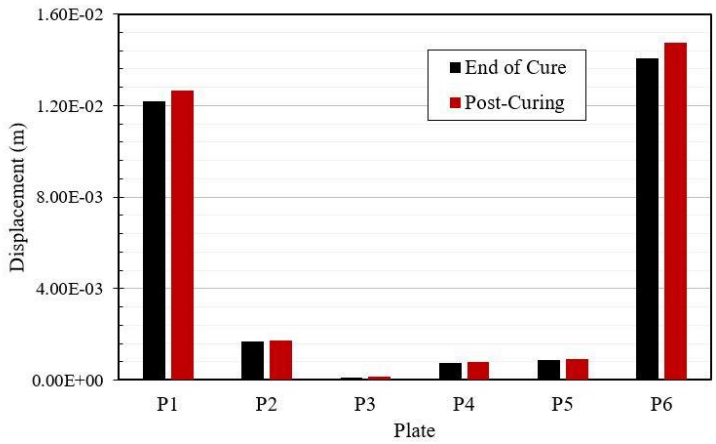

Figure 5.15. Displacement at steps 6 and 7

The maximum interlaminar stresses after the post-curing process are shown in Figure 5.16. Here, the maximum stress is observed on the quasi-isotropic laminate (Plate P4). However, this value decreases after the post-curing process. For the rest of the laminates, the stress increases

lightly. The maximum interlaminar stress in the angle-ply symmetric laminate (Plate P4) decreases during cool down. It is important to highlight that the location of the maximum stress changes in some of the plates. This table only considers the maximum magnitudes and is not describing the behavior of a specific node.

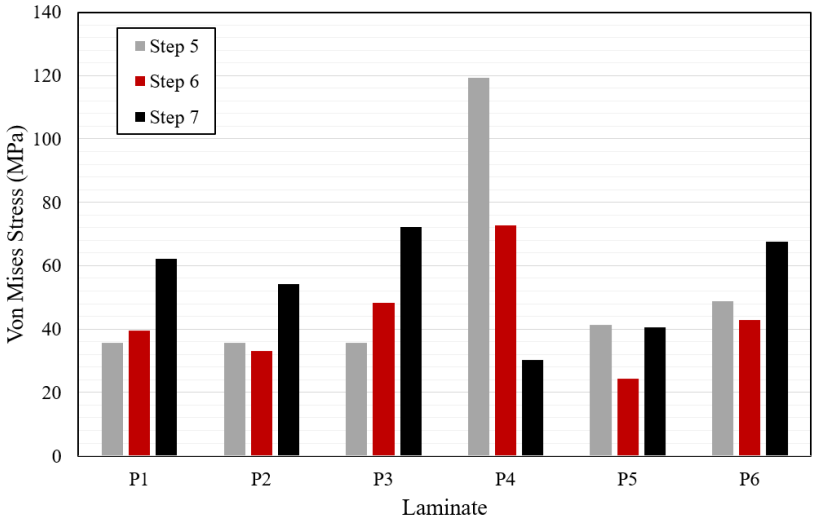

Figure 5.16. Stress at steps 5, 6 and 7.

5.5 Viscoelasticity Effects

The purpose of this section is to observe the effects of the cure-dependent viscoelastic model. The compared laminate is Plate P1. Here, the cure shrinkage and thermal expansion remain the same as in the previously analyzed models. However, the cure-dependent viscoelastic model is substituted by a linear elastic one. The values of the stiffness matrix are

the same as in Table 3.3. The stress buildup during the cure is presented in Figure 5.17. The stress buildup is higher in the viscoelastic model.

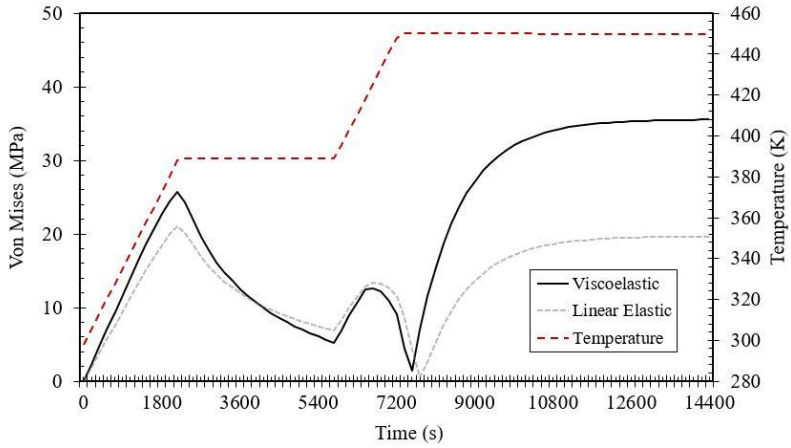

Figure 5.17. Viscoelastic effect on stress buildup during cure

Figure 5.18 presents the stress behavior after the cool down and post-curing process. Here, interlaminar stress values from Node 3 at Edge Y0 were obtained and plotted at three different times: end of second dwell temperature (Step 5), after cool down (Step 6), and at the end of post-curing (Step 7). This figure shows how the stress variation is much lower in the viscoelastic model.

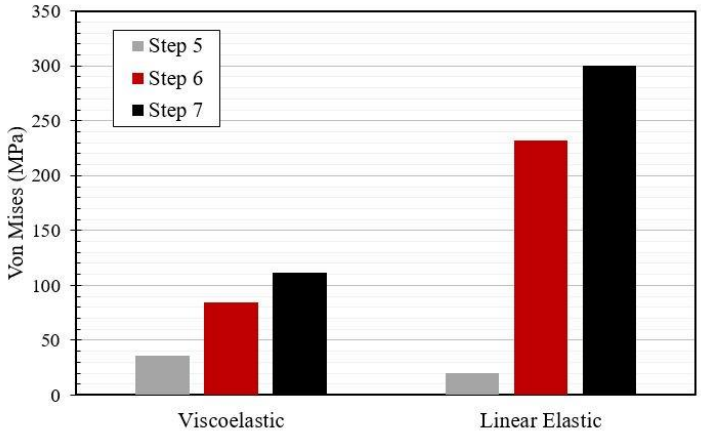

Figure 5.18. Stress behavior after curing in both models

5.6 Random Field Distribution

The effects of a stochastic distribution of random parameters during the curing process are analyzed in this section. Here, the cure kinetics parameters (A_1, A_2, A_3) and parameters related to the matrix-dominated stiffness development (E_2, G_{12}, G_{23}) are randomized. The stochastic behavior of the curing parameters produces a non-homogeneous distribution of the material shrinkage because this shrinkage is proportional to the rate of cure of the thermosetting material, as given in (2.55). Figure 5.19 shows the degree of cure rate random distribution over plate P1 after 30 minutes of cure. This can be also interpreted as the shrinkage distribution during the curing stage.

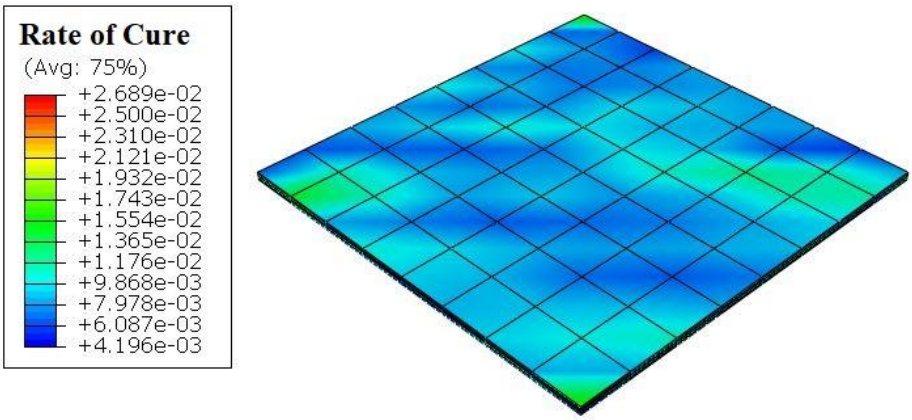

Figure 5.19. Cure rate random distribution

This random distribution has a clear effect over the stress buildup during the cure process as shown in Figure 5.20. Here the reference line (continuous red) is obtained from plate P1 as given earlier in Figure 5.1. It is important to note that for plates P1, P2 and P3, the stress buildup was the same in each node when the cure rate distribution was homogeneous. This changes when the parameters are randomized. The grey lines presented in this figure refer to different integration points of an element located at the Edge XY in the midplane of the laminate. It is evident how the interlaminar stresses can reach higher magnitudes than the ones expected in a homogenous analysis.

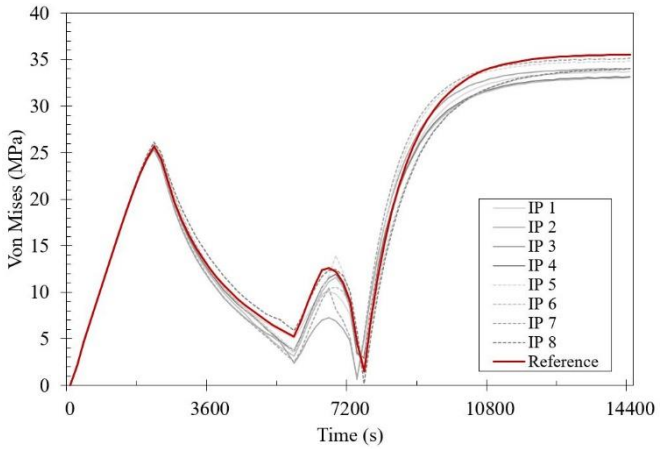

Figure 5.20. Stress buildup with random curing parameters

A sample of 10 laminates with the same ply configuration of P1 and considering a random distribution of the curing kinetics parameters were created to observe the stress variation during the cure process of the constrained laminate (Step 1 to Step 5). The results are presented in Figure 5.21. Here, the maximum and minimum values are the upper and lower limits of the dark grey area respectively. The standard deviation limits the light gray region. The mean value and the reference are represented with a red and a black continuous line respectively.

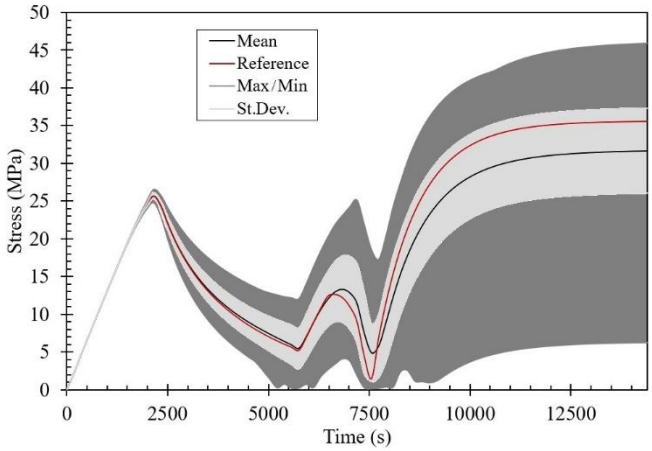

Figure 5.21. Stress buildup in the sample (Curing)

It is noteworthy how the stress buildup varies when random parameters are applied. In this case, the mean stress magnitude is 31.68 MPa, which is 10.86% smaller than the reference (35.54 MPa). However, the interlaminar stresses reach a maximum value of 45.94 MPa. This represents an increment of 29.26%.

When the stiffness-related parameters (E_2, G_{12}, G_{23}) are randomized, the variation of the stress magnitude tend to be smaller. An example of the stress development at each integration point is given in Figure 5.22

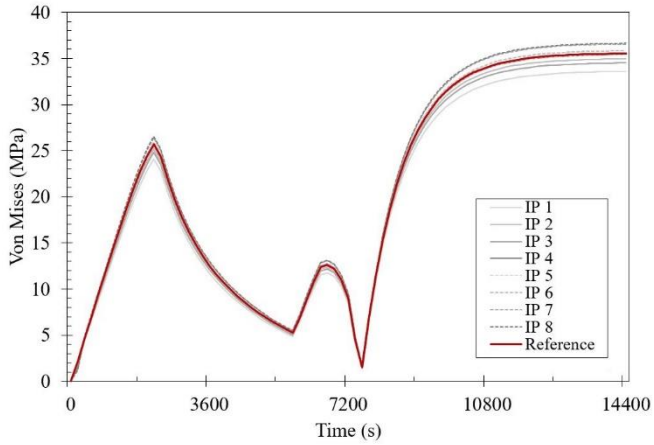

Figure 5.22. Stress buildup with random stiffness parameters

The stress variation in the sample, considering the parameters E_2, G_{12} and G_{23}, is shown in Figure 5.23

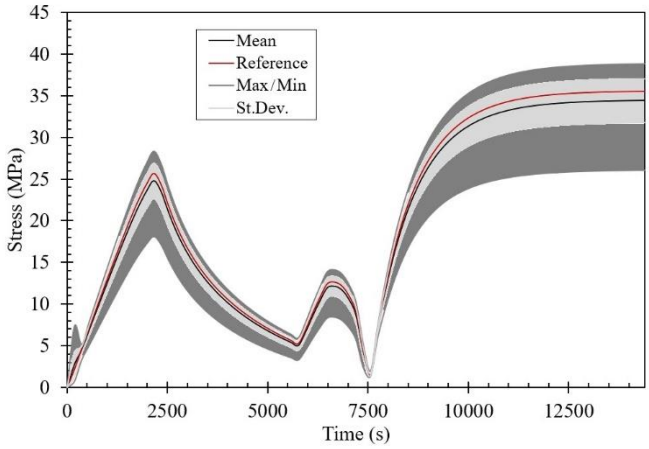

Figure 5.23. Stress buildup in the sample (Stiffness)

Finally, the same analysis is applied to the same sample. Here, all the six parameters are considered to have a random distribution. The results are presented in Figure 5.24

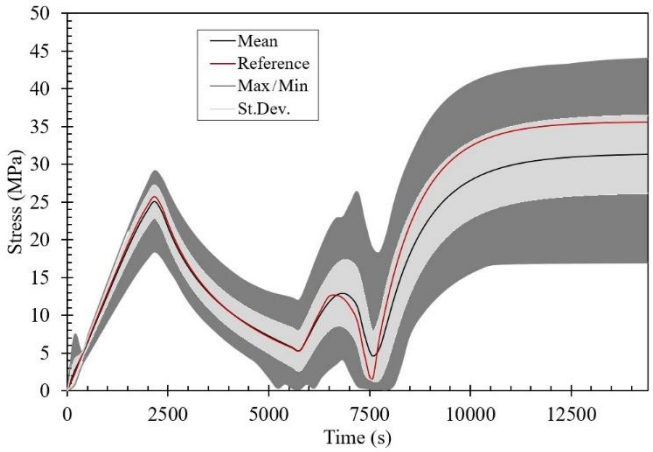

Figure 5.24. Stress buildup in the sample (All)

The results show that the residual stresses can reach a magnitude of 44.02 MPA, this is 23.86% higher than the refence value.

5.7 Experimental Results

In this case, the manufactured plates (Figure 5.25) were the ones that showed larger deformations in the computational results: P1 and P6.

Figure 5.25. Manufactured Plates

The raw data obtained from the 3D scanner is shown in Figure 5.26. After post-processing the raw data, the deformation is compared with the computational results.

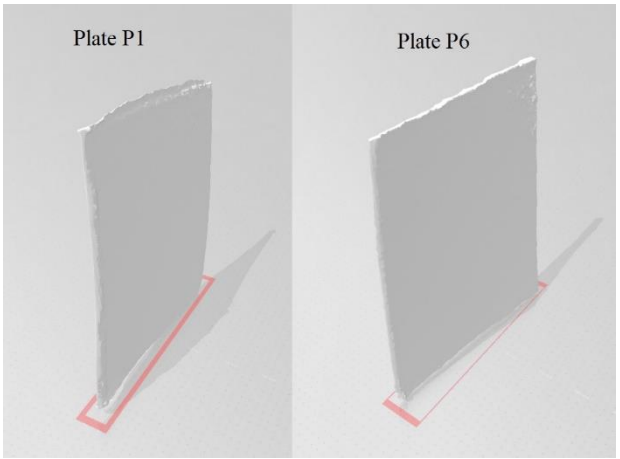

Figure 5.26. 3D scanner raw data

In the case of P1, Figure 5.27 shows the deformation observed from XZ plane. Here, the plate deformation has the shape of a convex curve. On the other side, Figure 5.28 shows it from the YZ plane. In both cases, the deformation takes the form of a concave curve.

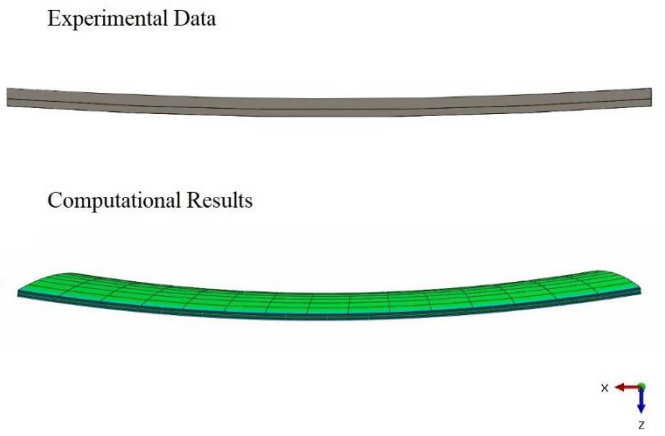

Figure 5.27. XZ Plane Comparison (P1)

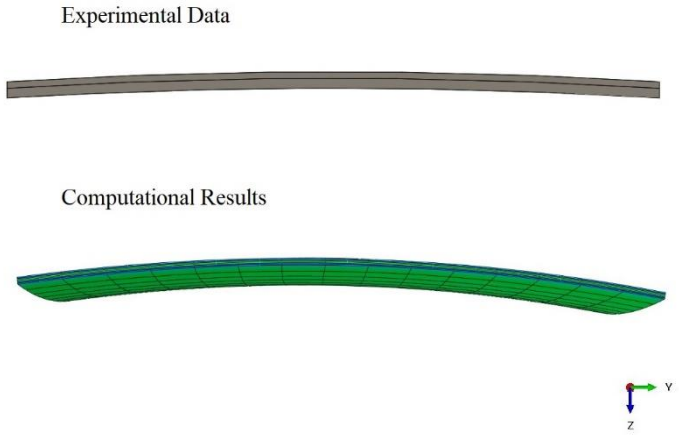

Figure 5.28. YZ Plane Comparison (P1)

For plate P6, the deformations observed from the XZ plane and YZ plane are given in Figure 5.29 and Figure 5.30, respectively. In this case, the plate shows a large displacement in one edge.

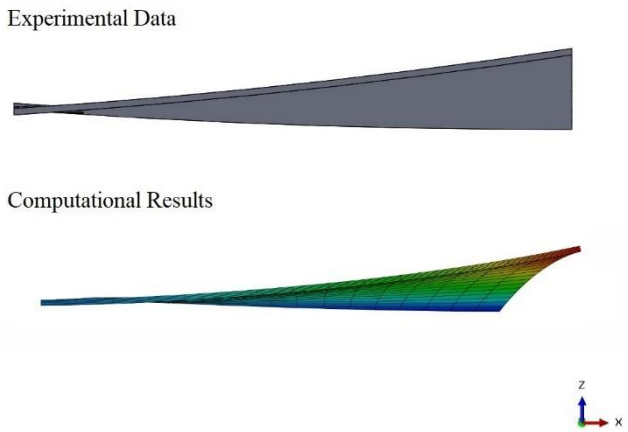

Figure 5.29. XZ Plane Comparison (P6)

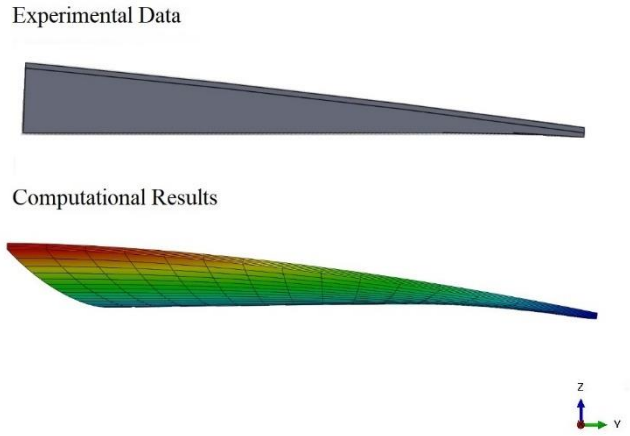

Figure 5.30. YZ Plane Comparison (P6)

As can be observed, the computational model shows good correspondence with the experimental data. The slight differences are the result of the post-processing of the raw data obtained from the 3D

Scanner. The magnitude of the displacement in *z* at the points X0, Y0 and XY (given in Figure 3.1) are listed in Table 5.4

Table 5.4. Displacement in mm over z-direction

	Computational		Experimental	
Point	P1	P6	P1	P6
X0	12.07	1.04	4.27	0.47
Y0	-12.17	14.73	-4.60	9.30
XY	0.38	-2.72	0.16	-1.64

The results differ in magnitude. This was expected, especially because of the thermal properties of the epoxy used in the experiment. In the case of the Hercules 3501-6 resin, the curing temperature reaches 177 ºC from where it cools down to a room temperature of 25 ºC. On the other side, the curing temperature of the R118 resin is 80 ºC. This difference affects the magnitude of the distortions related to the thermal expansion and contraction of the materials when cured.

In the case of P1, the magnitudes of X0 and Y0 are similar to each other but with different sign. Here, XY is relatively small. For the plate P6, the magnitude in Y0 is relatively large, while XY takes a negative value. These observations apply for the experimental and computational results. Showing that, despite of the magnitude difference, the data shows good correspondence.

6. Conclusions

This work presented an analysis of the process-induced stresses and distortions in unidirectional fiber composite panels with different laminate configurations. The computational method coupled the thermochemical and mechanical analysis to produce a cure-dependent viscoelastic model. Six different laminates were modeled to compare the material properties during and after the manufacturing process. This process was divided into four sections: in-mold curing, cooldown, post-curing, and final cooldown. During the in-mold curing (Section 1), the stress buildup was analyzed in several representative nodes of each laminate. The information related to plate distortion and nodal displacement was obtained from the cooldown stage (Section 2). A post-curing process was added (Sections 3 and 4) with the interest of observing the effect of this process over the different ply configurations. The analysis of each plate revealed that the laminate with a quasi-isotropic configuration $[-60/-30/0/30/60/90]$ undergoes the highest distortion. It also seems that for the cross-ply oriented laminates, the stress buildup is independent of the laminate configuration if the plate is constrained. At the cooldown stage, the smallest displacement (0.12

mm) was observed in the plate with symmetric cross-ply configuration $[90_2/0]_s$. However, this plate was highly affected by the post-curing process, where the distortion exhibited a distortion increase of 23.31%.

The post-curing process increased the magnitude of the interlaminar residual stress in most of the laminates. In the case of the antisymmetric angle ply laminate this value increased by 78.78%. On the other hand, the stress in the quasi-isotropic laminate decreased by 19.59%.

The comparison of the viscoelastic and linear elastic models revealed that the stress buildup during the curing process is higher in a viscoelastic model. Here, the maximum stress of the elastic model was 80.76% lower. However, after the plates are released and subjected to the cooldown and post-curing, the stresses of the linear elastic model reach higher values than in the viscoelastic one. The results show that stress can be 62.84% higher in the elastic model.

In a plate with a cross ply configuration, the interlaminar stresses have the same magnitude in all the nodes analized. However, when the shrinkage of the material is non-homogeneous, variations in the stresses are found. Hence, the interlaminar stress development during the curing process varies when a stochastic model is considered. The magnitude of the maximum stress increased in 23.86%. This shows the importance of

considering the randomness of the parameters when modeling the manufacture process of composite materials.

This work was focused on a macroscale analysis of the residual stresses during cure. Nevertheless, a microscale analysis of a degree of the cure-dependent viscoelastic model applied to CLT may add important results. That is out of the scope of this thesis but is an open gate for future works.

Bibliography

1. Williams, J.C. and E.A. Starke, *Progress in structural materials for aerospace systems11The Golden Jubilee Issue—Selected topics in Materials Science and Engineering: Past, Present and Future, edited by S. Suresh.* Acta Materialia, 2003. **51**(19): p. 5775-5799.
2. Gibson, R.F., *Principles of Composite Material Mechanics*. 2016, Boca Raton, FL, USA: CRC Press.
3. Buhl, H., *Advanced Aerospace Materials*. 1992, Berlin: Springer-Verlag.
4. E., W.M.K.a.J., *Improved Langmoir probe surface coatings for the Cassini satellite.* Thin Solid Films, 1992. **220**: p. 315-320.
5. Brogren, M., *Titanium-Aluminum-Nitride coatings for satellite temperature control.* Thin Solid Films, 2000. **370**(1-2): p. 268-277.
6. He, P., X. Yue, and J.H. Zhang, *Hot pressing diffusion bonding of a titanium alloy to a stainless steel with an aluminum alloy interlayer.* Materials Science and Engineering: A, 2008. **486**(1-2): p. 171-176.
7. Baker, A., *Composite Materials for Aircraft Structures*. Second Edition ed. 2004, Virginia, USA: American Institute of Aeronautics and Astronautics, Inc.
8. Guo, Q., *Thermosets: Structure, properties and applications*. 2012, Cambridge, UK: Woodhead Publishing Limited.
9. Hemendra, K.J., *Laminated Composite Stiffened Panels: Applications and Behaviour*, in *Civil Engineering Conference Innovation Without Limit*. 2009: NIT Hamirpur. p. 89-96.
10. Ye, L., et al., *Functionalized composite structures for new generation airframes: a review.* Composites Science and Technology, 2005. **65**(9): p. 1436-1446.
11. Megson, T.H.G., *Aircraft Structures for engineering students*. 2017, Cambridge, MA, USA: Elsevier Ltd.
12. Soutis, P.E.I.a.C., *Polymer Composites in he Aerospace Industry*. 2015, Sawston, Cambridge, United Kingdom: Elsevier Ltd.
13. . 2020.
14. Museum, E. *The Spruce Goose*. 2018; Available from: www.evergreenmuseum.org/the-spruce-goose.

15. Association, A.C.M. *Composites Manufacturing Processes*. 2020; Available from: http://compositeslab.com/composites-manufacturing-processes/.
16. Kim, S.-Y., et al., *Mechanical properties and production quality of hand-layup and vacuum infusion processed hybrid composite materials for GFRP marine structures.* International Journal of Naval Architecture and Ocean Engineering, 2014. **6**(3): p. 723-736.
17. Advani, S.G.a.H., K. T., *Manufacturing techniques for polymer matrix composites*. 2012, Cornwall, UK: Woodhead Publishing Limited.
18. Péron, M., et al., *Thermo-mechanical characterization of a thermoplastic composite and prediction of the residual stresses and lamina curvature during cooling.* AIP Conference Proceedings, 2017.
19. Chen, W. and Z. Dianyun, *A micromechanics-based processing model for predicting residual stress in.* Composite Structures, 2018(204): p. 153-166.
20. Abouhamzeh, M., J. Sinke, and R. Benedictus, *Prediction Models for Distortions and Residual Stresses in Thermoset Polymer Laminates: An Overview.* Journal of Manufacturing and Materials Processing, 2019. **3**(4): p. 87.
21. Benavente, M. and L. Marcin, *Numerical Analysis of viscoelastic process-induced residual distoritons during manufacturing and post-curing.* Composites Part A, 2018.
22. Takagaki, K., S. Minakuchi, and N. Takeda, *Process-induced strain and distortion in curved composites. Part II: Parametric study and application.* Composites Part A: Applied Science and Manufacturing, 2017. **103**: p. 219-229.
23. Wisnom, M.R., et al., *Mechanisms generating residual stresses and distortion during manufacture of polymer–matrix composite structures.* Composites Part A: Applied Science and Manufacturing, 2006. **37**(4): p. 522-529.
24. Shokrieh, M. and K.S. M., *Theoretical and Experimental Studies on Residual Stresses in Laminated Polymer Composites.* Journal of Composite Materials, 2005. **39**(24): p. 2213-2225.
25. Ding, A., S. Li, and L. Zu, *A three-dimensional thermo-viscoelastic analysis of process-induced.* Composite Structures, 2015. **129**: p. 60-69.

26. Yuan, Z., et al., *Evolution of curing residual stresses in composite using multi-scale method.* Composites Part B, 2018(155): p. 59-61.
27. Zhang, D. and A.M. Waas, *A micromechanics based multiscale model for nonlinear.* Acta Mechanica, 2014(225): p. 1391-1417.
28. O'Brien, D., P. Mather, and S. White, *Viscoelastic Properties of an Epoxy Resin.* Journal of Composite Materials, 2001. **35**(10): p. 883-904.
29. Christian Heinrich, M.A., Alan S. Wineman, John Kieffer, Anthony M. Waas, Khaled W. Shahwan, *Generation of heat and stress during the cure of polymers used.* International Journal of Engineering Science, 2011.
30. Abouhamzeh, M., J. Sinke, and R. Benedictus, *Investigation of curing effects on distortion of fibre metal laminates.* Composite Structures, 2014. **122**: p. 456-522.
31. Benavente, M., et al., *Viscoelastic distortion in asymmetric plates during post curing.* Composites Part A: Applied Science and Manufacturing, 2017. **103**: p. 122-130.
32. Svanbergn, J. and J. Holmber, *An experimental investigation on mechanisms for manufacturing induced shape distortions in homogeneous and balanced laminates.* Composites Part A: Applied Science and Manufacturing, 2001. **32**(6): p. 827-838.
33. White, S.R. and H.T. Hahn, *Cure Cycle Optimization for the Reduction of Processing-Induced Residual Stresses in Composite Materials.* Journal of Composite Materials, 1993. **27**(14): p. 1352-1378.
34. Sourour, S. and M.R. Kamal, *Differential scanning calorimetry of epoxy cure: Isothermal cure kinetics.* Thermochimica Acta, 1976. **14**: p. 41-59.
35. Kamal, M.R., *Thermoset Characterization for Moldability Analysis.* Polymer Engineering and Science, 1974. **14**(3).
36. Shin, D.D. and H.T. Hahn, *A consistent cure kinetic model for AS4/3502 graphite/epoxy.* Composites Part A: Applied science and manufacturing, 2000. **31**: p. 991-999.
37. Scott, E.S., Z., *Estimation of Kinetic Parameters Associated with the Curing of Thermoset Resins. Part I: Theroetical Investigation.* Polymer Engineering & Science, 1993. **33**(18).

38. White, S.R. and H.T. Hahn, *Mechanical property and residual stress development during cure of a graphite/BMI composite.* Polymer Engineering & Science, 1990. **30**(22).
39. Lee, W.I., A.C. Loos, and G.S. Springer, *Heat of reaction, degree of cure, and viscosity of Hercules 3501-6 resin.* Journal of Composite Materials, 1982. **16**: p. 510.
40. Ozisik, M.N., *Heat Conduction*. 1993, New York, NY, USA: John Wiley & Sons, Inc.
41. Springer, G.S. and S.W. Tsai, *Thermal conductivities of unidirectional materials.* Journal of Composite Materials, 1967. **1**: p. 166-173.
42. Brinson, H. and C. Brinson, *Polymer Engineering Science and Viscoelasticity An Introduction*. 2008, New York, NY, USA: Springer.
43. Shay, M.T. and W.J. MacKnight, *Introduction to Polyemer Viscoelasticity*. 2005, Hoboken, NJ, USA: Wiley Interscience.
44. Fancey, K.S., *A mechanical model for creep, recovery and stress relaxation in polymeric materials.* Journal of Materials Science, 2005: p. 1-5.
45. Syed, A.A., *Thermoforming of Sunfle and Multilayer Laminates*. 2014, Waltham, MA, USA: Elsevier.
46. Gillani, A., *Development of Material Model Subroutimes for Linear and Non Linear Response of Elastomers*. 2018, University of Western Ontario: Ontario.
47. Saad, M.H., *Continuum Mechanics Modeling of Material Behavior*. 2019, San Diego, CA, USA: Elsevier.
48. Wang, X., K. Zhao, and H. Zhao, *Finite Element Simulation of Biofilm Viscoelastic Behavior Under Various Loadings.* Journal of Mechanics in Medicine and Biology, 2018.
49. Nedjar, B., *A time dependent model for unidirectional fibre-reinforced composites with viscoelastic matrices.* International Journal of Solids and Structures, 2011.
50. Drozdov, A., *Viscoelastic Structures: Mechanics of Growth and Aging*. 1998, CA, USA: Academic Press Limited.
51. Christensen, R.M., *Theory of Viscoleasticity: An Introduction*. 1982, NY, USA: Academic Press.
52. Hernández, W.P., et al., *Thermorheologically simple materials: A bayesian framework for model calibration and validation.* Journal of Sound and Vibration, 2017. **402**: p. 14-30.

53. O'Brien, D.J., P.T. Mather, and S.R. White, *Viscoelastic Properties of an Epoxy Resin during Cure.* Journal of Composite Materials, 2001. **35**(10): p. 883-904.
54. Lee, W.L., A., *Heat of Reaction, Degree of Cure, and Viscosity of Hercules 3501-6 Resin.* Journal of Composite Materials, 1982. **16**: p. 510.
55. Courtois, A., et al., *Viscoelastic behavior of an epoxy resin during cure below the glass transition temperature: Characterization and modeling.* Journal of Composite Materials, 2018. **53**(2): p. 155-171.
56. Kim, Y.K. and S.R. White, *Stress relaxation behavior of 3501-6 epoxy resin during cure.* Polymer Engineering and Science, 1996. **36**(23): p. 2852-2862.
57. Heinrich, C., et al., *The role of curing stresses in subsequent response, damage and failure of textile polymer composites.* Journal of the Mechanics and Physics of Solids, 2013. **61**(5): p. 1241-1264.
58. Oden, J.T.B., T.; Babuska, I; Hughes, T.J.R., *Researh directions in computational mechanics.* Computer methods in applied mechanics and engineering, 2003. **192**: p. 913-922.
59. Stefanou, G., *The stochastic finite element method: Past, present and future.* Computer Methods in Applied Mechanics and Engineering, 2009. **198**(9-12): p. 1031-1051.
60. Zhang, J., *Orthogonal series expansions of random fields in reliability analysis.* Journal of Engineering Mechanics, 1994. **120**(12).
61. Shang, S. and G.J. Yun, *Stochastic finite element with material uncertainties: Implementation in a general purpose simulation program.* Finite Elements in Analysis and Design, 2013. **64**: p. 65-78.
62. Allaix, D.L. and V.I. Carbone, *Discretization of 2D random fields: A genetic algorithm approach.* Engineering Structures, 2009. **31**(5): p. 1111-1119.
63. Ghanem, R.S., Pol, *Stochastic Finite Elements A spectral Approach*. 2003, NY, USA: Dover Publications, Inc.
64. Zhu, F.-Y., et al., *Probabilistic multiscale modeling of 3D randomly oriented and aligned wavy CNT nanocomposites and RVE size determination.* Composite Structures, 2018. **195**: p. 265-275.

65. White, S.R. and Y.K. Kim, *Process-induced residual stress analysis of AS4/3501-6 composite material*. Mechanics of Composite Materials and Structures, 1998. **5**(2): p. 153-186.

국문초록

확률적 열화학 점탄성 모델을 이용한 탄소 섬유 강화 라미네이트 복합 재료의 가상 RTM 제조 시뮬레이션.

세바스티안 레오나르도 블랑코 로자스
항공우주공학과 항공우주공학전공
서울대학교 대학원

복합 재료는 매트릭스(matrix)의 경화 속도에 관련된 수축 과정을 거친다. 재료 열팽창에 더해지는 이러한 수축 효과는 재료의 기계적 성능에 부정적인 영향을 미치는 기하학적 비틀림과 잔류 층간 응력을 초래한다.

본 연구는 항공 우주 구조물에 사용되는 탄소 섬유 강화 복합재료 라미네이트(laminate)에 제조 공정이 미치는 영향을 분석한다. 여기서, 경화 정도 및 시간 의존적 특성을 갖는 점탄성 재료를 모델링하는 컴퓨터 시뮬레이션 툴이 구현된다. 또한, 결과의 신뢰성을 높이기 위해

경화 동역학 파라미터의 랜덤 특성을 고려하는 확률론적 모델이 구현된다.

이 모델은 열화학 및 기계 공정을 결합하는 다중 물리 시스템으로 구성된다. 먼저, 열전달 해석은 Fourier 의 열전도 지배 방정식과 Kamal 의 경화 동역학 모델을 통해 수행된다. 그런 다음 점탄성 거동을 나타내기 위해 아홉개의 요소(9-element)로 일반화 된 Maxwell 모델이 구현된다. 재료모델이 경화 모델과 점탄성 모델 만으로 표현될 수 있는 이유는 열경화성 수지가 열/유동학적으로 간단한 성질을 가지기 때문이다. 여기서, 재료의 온도 및 경화 정도에 따라 변화하는 응력 완화 시간을 얻기 위해 환산 인자(shift factor)가 적용된다. 재료의 확률론적 거동을 나타내는 랜덤 필드(random field)는 Monte Carlo 시뮬레이션으로 Karhunen-Loève Expansion 방법을 구현하여 만들어진다.

이번 연구에서 모델링하는 제조 공정은 진공 레진 전달 몰딩(vacuum-assisted transfer molding, VARTM)과 그 후처리 과정으로 구성되었다. 이 공정을 모방하기 위한 열기계적 경계 조건은 4 단계로 나뉜다. 첫 번째는 경화 단계이다. 여기서 플레이트는 몰드(mold)에 구속되고 몰드 표면에서 열 전도가 일어난다. 두 번째 단계는 플레이트가 몰드에서 분리되어 대류에 의해 상온으로 냉각되는

상태이다. 세 번째 단계는 냉각된 플레이트를 오븐(강제 열 대류)에 넣는 것이다. 마지막으로, 플레이트는 두 번째 단계에서와 같이 냉각되도록 방치된다. 이 제조 공정에서 발생하는 응력과 비틀림은 플라이 구성이 다른 6 개의 플레이트에 대해 분석되었다.

시뮬레이션 결과 준 등방성 라미네이트 [−60 / −30 / 0 / 30 / 60 / 90]가 가장 높은 층간 응력과 비틀림을 겪었고 그 다음으로는 비대칭 크로스−플라이(cross−ply) 라미네이트$[90_3/0_3]$ 가 높은 층간 응력과 비틀림을 기록했다. 또한, 후처리 공정은 대부분의 비대칭 앵글 플라이(angle ply) 라미네이트에서 층간 잔류 응력을 증가시키는 것으로 밝혀졌다.

경화 의존 점탄성 모델의 타당성은 선형 탄성 재료모델과의 비교를 통해 검증된다. 점탄성 모델은 선형 탄성 모델에 비해 경화 단계에서는 더 높은 응력을 예측하지만 플레이트가 몰드에서 분리되면 더 낮은 응력을 보여준다. 마지막으로, 경화 동역학 파라미터의 랜덤 특성을 고려함에 따른 효과는 크로스−플라이 라미네이트의 경화 단계에서 관찰되었다. 랜덤 특성을 고려한 모델은 이 효과를 고려하지 않은 모델에 비해서 최대 23.86% 더 높은 응력을 가질 수 있음이 관측되었다. 이는 경화 공정과 관련된 랜덤 특성을 고려하는 것이 복합재료 경화 공정을 해석하는 데에 매우 중요 함을 보여준다.

Keywords : 점탄성, 경화 동역학, 복합재 라미네이트, 잔류응력, 라미네이트 비틀림, 유한요소해석, 확률적 거동, 확률장

Student Number : 2018-27407

Appendix

Appendix A. Laminate Stiffness Matrix

The matrices used in CLT are computed using commercial software MATLAB, the lamina stiffness matrix for unidirectional AS/3501-6 carbon epoxy is obtained from the literature [2]

$$[Q_{ij}] = \begin{bmatrix} 138.8 & 2.72 & 0 \\ 2.72 & 9.05 & 0 \\ 0 & 0 & 6.9 \end{bmatrix} GPa \tag{A.1}$$

The extensional stiffness matrix [**A**] obtained from Eq. (2.74), the bending-extension coupling matrix [**B**] from Eq. (2.75) and the bending stiffness matrix [**D**] comes from (2.76).

The extensional, coupling and bending matrices for the asymmetric cross-ply laminate P1 are presented in equations 1, 2 and 3 respectively

$$[A_{ij}^{A}] = \begin{bmatrix} 221.78 & 8.16 & 0 \\ 8.16 & 221.78 & 0 \\ 0 & 0 & 20.70 \end{bmatrix} \times 10^{6} \tag{A2}$$

$$[B_{ij}^{A}] = \begin{bmatrix} 1.46 & 0 & 0 \\ 0 & -1.46 & 0 \\ 0 & 0 & 0 \end{bmatrix} \times 10^{5} \tag{A3}$$

$$[D_{ij}^{A}] = \begin{bmatrix} 166.33 & 6.12 & 0 \\ 6.12 & 166.33 & 0 \\ 0 & 0 & 15.52 \end{bmatrix} \tag{A4}$$

In the same way, the matrices for each laminate are shown from Eq. (A5) to (A19).

In the case of the asymmetric cross-ply laminate P2, the matrices are:

$$\left[A_{ij}^{B}\right] = \begin{bmatrix} 221.78 & 8.16 & 0 \\ 8.16 & 221.78 & 0 \\ 0 & 0 & 20.70 \end{bmatrix} \times 10^{6} \quad \text{(A5)}$$

$$\left[B_{ij}^{B}\right] = \begin{bmatrix} 4.87 & 0 & 0 \\ 0 & -4.87 & 0 \\ 0 & 0 & 0 \end{bmatrix} \times 10^{4} \quad \text{(A6)}$$

$$\left[D_{ij}^{B}\right] = \begin{bmatrix} 166.33 & 6.12 & 0 \\ 6.12 & 166.33 & 0 \\ 0 & 0 & 15.52 \end{bmatrix} \quad \text{(A7)}$$

Symmetric cross-ply laminate P3:

$$\left[A_{ij}^{C}\right] = \begin{bmatrix} 156.90 & 8.16 & 0 \\ 8.16 & 286.65 & 0 \\ 0 & 0 & 20.70 \end{bmatrix} \times 10^{6} \quad \text{(A8)}$$

$$\left[B_{ij}^{C}\right] = \begin{bmatrix} 0 & 0 & 0 \\ 0 & 0 & 0 \\ 0 & 0 & 0 \end{bmatrix} \quad \text{(A9)}$$

$$\left[D_{ij}^{C}\right] = \begin{bmatrix} 31.18 & 6.12 & 0 \\ 6.12 & 301.49 & 0 \\ 0 & 0 & 15.52 \end{bmatrix} \quad \text{(A10)}$$

Symmetric angle-ply laminate P4:

$$\left[A_{ij}^{D}\right] = \begin{bmatrix} 229.25 & 65.57 & 64.88 \\ 65.57 & 99.50 & 64.88 \\ 64.88 & 64.88 & 78.11 \end{bmatrix} \times 10^{6} \quad \text{(A11)}$$

$$\left[B_{ij}^{D}\right] = \begin{bmatrix} 0 & 0 & 0 \\ 0 & 0 & 0 \\ 0 & 0 & 0 \end{bmatrix} \quad \text{(A12)}$$

$$\left[D_{ij}^{D}\right] = \begin{bmatrix} 109.55 & 68.31 & 70.28 \\ 68.31 & 98.73 & 70.28 \\ 70.28 & 70.28 & 77.71 \end{bmatrix} \quad \text{(A13)}$$

Antisymmetric angle-ply laminate P5:

$$\left[A_{ij}^{E}\right] = \begin{bmatrix} 254.51 & 72.74 & 0 \\ 72.74 & 59.88 & 0 \\ 0 & 0 & 85.28 \end{bmatrix} \times 10^{6} \quad \text{(A14)}$$

$$\left[B_{ij}^{E}\right] = \begin{bmatrix} 0 & 0 & -30.39 \\ 0 & 0 & -11.75 \\ -30.39 & -11.75 & 0 \end{bmatrix} \times 10^{3} \quad \text{(A15)}$$

$$\left[D_{ij}^{E}\right] = \begin{bmatrix} 190.88 & 54.56 & 0 \\ 54.56 & 44.91 & 0 \\ 0 & 0 & 63.96 \end{bmatrix} \quad \text{(A16)}$$

Quasi-isotropic laminate P6:

$$\left[A_{ij}^{F}\right] = \begin{bmatrix} 178.72 & 51.21 & 0 \\ 51.21 & 178.72 & 0 \\ 0 & 0 & 63.75 \end{bmatrix} \times 10^{6} \quad \text{(A17)}$$

$$\left[B_{ij}^{F}\right] = \begin{bmatrix} -3.79 & -1.08 & 3.59 \\ -1.08 & 5.94 & 4.83 \\ 3.59 & 4.83 & -1.08 \end{bmatrix} \times 10^{4} \quad \text{(A18)}$$

$$\left[D_{ij}^{F}\right] = \begin{bmatrix} 62.85 & 36.62 & -17.96 \\ 36.62 & 208.82 & -24.18 \\ -17.96 & -24.18 & 46.02 \end{bmatrix} \quad \text{(A19)}$$

Appendix B. Thermochemical analysis code

The results of the stress distribution in each plate of the sample using random parameters are presented in this appendix.

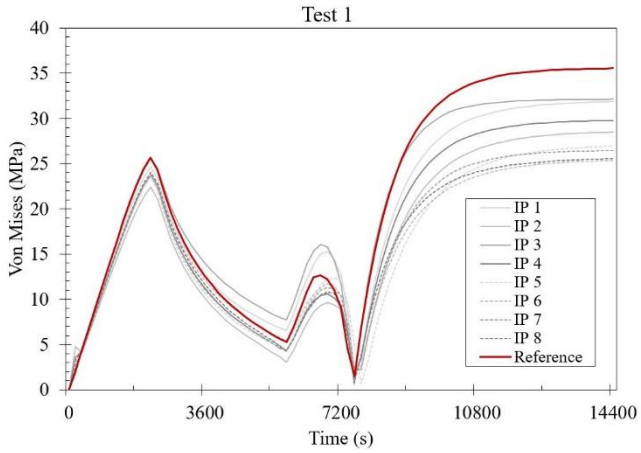

Figure B 1. Stresses in Test 1

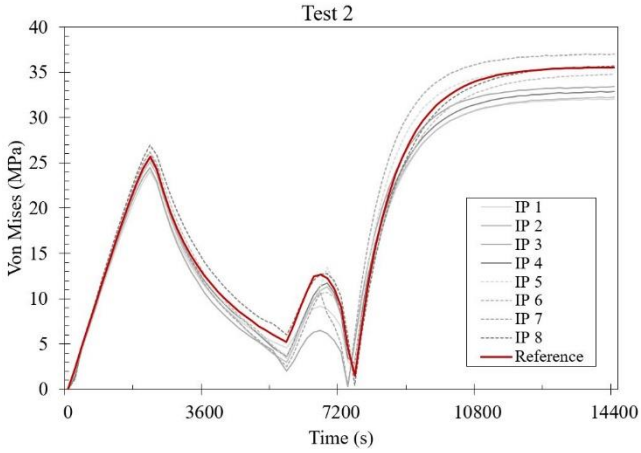

Figure B 2. Stresses in Test 2

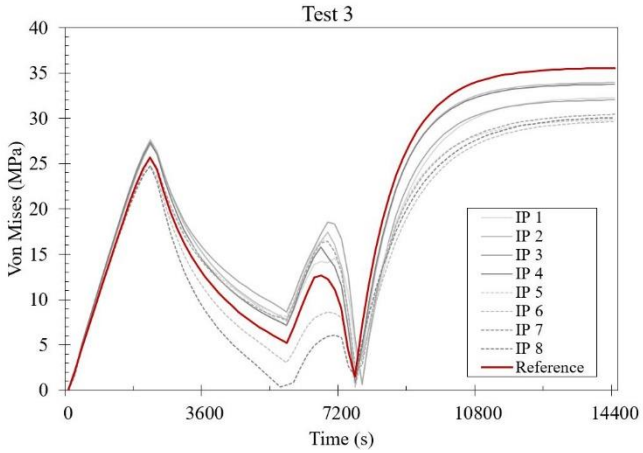

Figure B 3. Stresses in Test 3

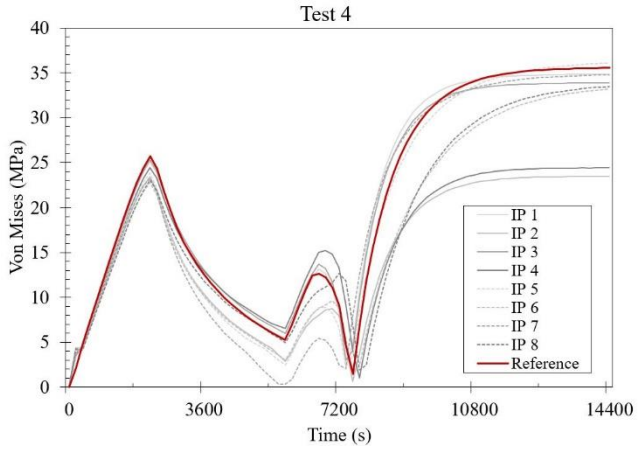

Figure B 4. Stresses in Test 4

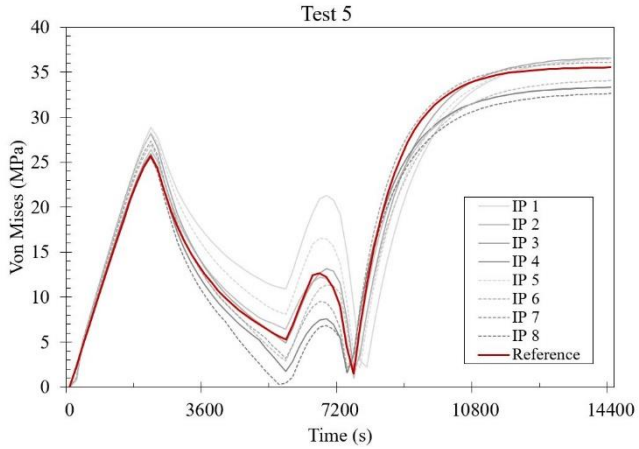

Figure B 5. Stresses in Test 5

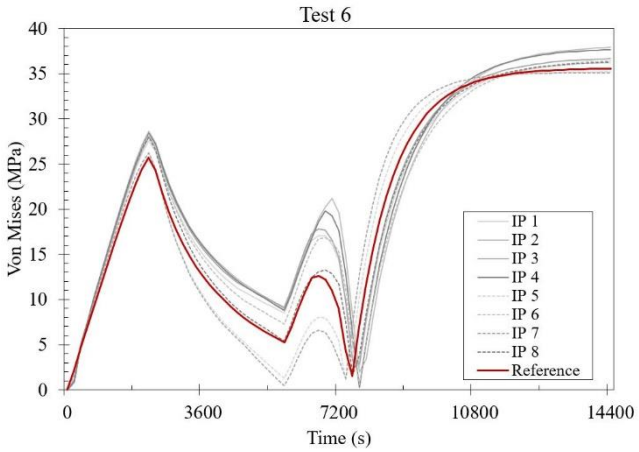

Figure B 6. Stresses in Test 6

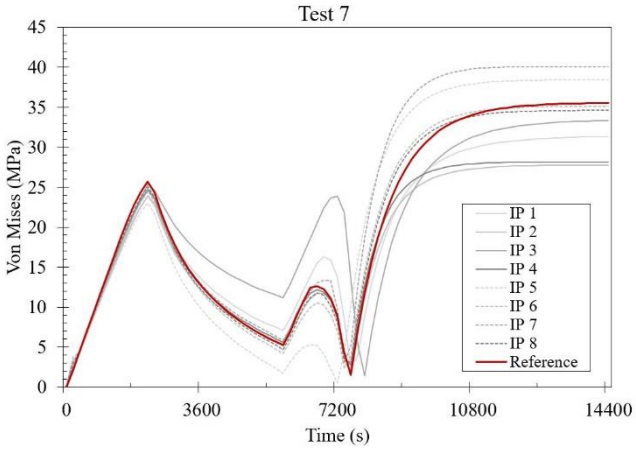

Figure B 7. Stresses in Test 7

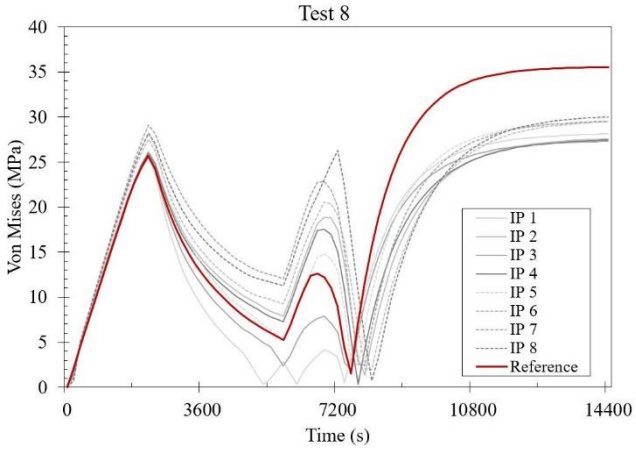

Figure B 8. Stresses in Test 8

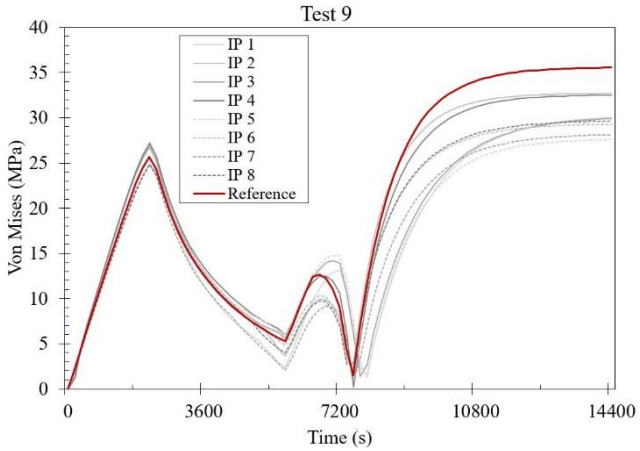

Figure B 9. Stresses in Test 9

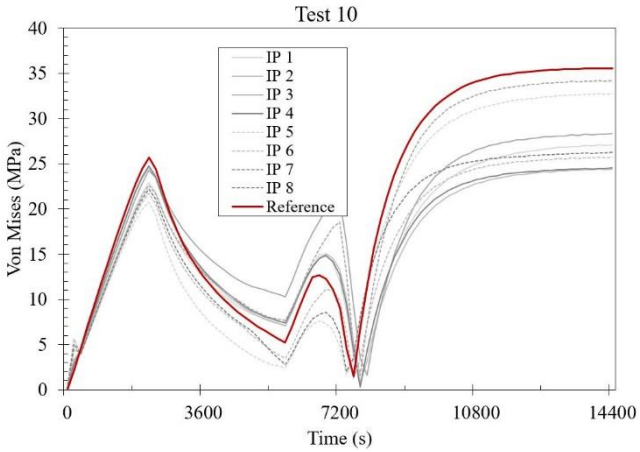

Figure B 10. Stresses in Test 10